J. Fluid Mech. (1999), *vol.* 385, *pp.* 325–358. Printed in the United Kingdom

Direct numerical simulations of bubbly flows
Part 2. Moderate Reynolds number arrays

By ASGHAR ESMAEELI AND GRÉTAR TRYGGVASON

Department of Mechanical Engineering and Applied Mechanics, The University of Michigan,
Ann Arbor, MI 48109, USA

(Received 2 January 1997 and in revised form 13 November 1998)

Direct numerical simulations of the motion of two- and three-dimensional finite Reynolds number buoyant bubbles in a periodic domain are presented. The full Navier–Stokes equations are solved by a finite difference/front tracking method that allows a fully deformable interface between the bubbles and the ambient fluid and the inclusion of surface tension. The rise Reynolds numbers are around 20–30 for the lowest volume fraction, but decrease as the volume fraction is increased. The rise of a regular array of bubbles, where the relative positions of the bubbles are fixed, is compared with the evolution of a freely evolving array. Generally, the freely evolving array rises slower than the regular one, in contrast to what has been found earlier for low Reynolds number arrays. The structure of the bubble distribution is examined and it is found that while the three-dimensional bubbles show a tendency to line up horizontally, the two-dimensional bubbles are nearly randomly distributed. The effect of the number of bubbles in each period is examined for the two-dimensional system and it is found that although the rise Reynolds number is nearly independent of the number of bubbles, the velocity fluctuations in the liquid (the Reynolds stresses) increase with the size of the system. While some aspects of the fully three-dimensional flows, such as the reduction in the rise velocity, are predicted by results for two-dimensional bubbles, the structure of the bubble distribution is not. The magnitude of the Reynolds stresses is also greatly over-predicted by the two-dimensional results.

1. Introduction

In two earlier papers (Esmaeeli & Tryggvason 1996, 1998) we used direct numerical simulations to examine the motion of a number of freely evolving bubbles at low, but finite Reynolds numbers (around 1–2, depending on volume fraction and dimensionality). The simulations showed that a regular array is unstable and that it breaks up through two-bubble interactions of the ‘drafting, kissing, and tumbling’ type. Although the motion of a regular array at $O(1)$ Reynolds numbers is fairly similar to Stokes flow, the evolution of the free array differs because of the strong two-bubble interactions. In this paper we continue our investigations by looking at a higher Reynolds number flow.

The need for direct numerical simulations of the full time-dependent Navier–Stokes equations is widely recognized by multiphase flow researchers. The computational difficulties in dealing with the unsteady motion of moving phase boundaries have, however, limited computational modelling to relatively simple systems where considerable simplifications are made in order to make simulations feasible. For flows where one phase is dispersed in another one in the form of bubbles, drops, or particles, these approximations can be put in three categories: potential flow models for high Reynolds number flows, Stokes flow models for low Reynolds number flows, and point particle models for dilute intermediate Reynolds number flows. These are discussed in the remainder of this Section.

For spherical particles in Stokes flow, Brady and collaborators (see Brady 1993, for a review) simulated the motion of many particles in fully three-dimensional geometries using 'Stokesian Dynamics'. They have used the result to explore the behaviour of various bulk quantities as well as the fundamental interactions between the particles. Similar techniques have recently been used by other authors (see Ladd 1997, for example). Simulations of deformable drops are more recent, and a few authors have used boundary integral methods to simulate the motion of a few drops. Zhou & Pozrikidis (1993, 1994) followed the evolution of up to twelve two-dimensional drops in shear flows, Manga & Stone (1993) examined the collision of two three-dimensional drops, and Loewenberg & Hinch (1996) examined the motion of eight three-dimensional drops in a shear flow.

To model the motion of bubbles at high Reynolds numbers, Sangani & Didwania (1993) and Smereka (1993) assumed spherical bubbles moving in a potential flow. Viscous drag was accounted for by computing the viscous dissipation of the potential flow. These simulations have shown, among other things, that buoyant bubbles tend to form large horizontal clusters. Such clusters have not been seen experimentally and the applicability of this model to real flows is not completely clear at present. For deformable particles a few authors have applied boundary integral techniques to follow the motion of a few bubbles. See Chahine (1994) and Blake & Tong (1995), for example.

For intermediate Reynolds numbers, several authors (including Squires & Eaton 1990; Wang & Maxey 1993; Truesdell & Elghobashi 1994) have examined the motion of particles (bubbles, drops, or solid objects) in finite Reynolds number flows by representing the dispersed phase by points moving in an otherwise constant-density flow. The force on each point particle is specified by analytical models for very low and very high Reynolds numbers (Stokes flow and potential flow) and by empirical correlations for finite values. In some cases the particles are assumed to have no effect on the fluid flow, but in other cases the forces from the particles are added to the right-hand side of the Navier–Stokes equations. The fundamental assumption is that the length scales of the fluid motion are much larger than the size of the particles and that there are no direct particle–particle interactions. Recent computational studies have provided reliable correlations for the forces on spherical bubbles, see Mei (1996) and Magnaudet (1997). Furthermore, the wake is usually neglected completely. Recently, however, Pan & Banerjee (1997) and Maxey & Patel (1997) have presented simulations where the particle size and its wake are accounted for by distributing the effect of the particle over a few grid points. See also Climent & Magnaudet (1997) for an attempt to account for wake effects.

While the point particle approximation is likely to be a good one for very low volume fractions, and while the potential flow approximation may be a reasonable one for spherical bubbles at high enough Reynolds numbers, both approximations are certainly insufficient for high volume fraction flow of bubbles, drops, and particles at intermediate Reynolds numbers. Here, it is necessary to solve the full Navier–Stokes equations for the unsteady flow around each moving particle, resolving in detail all boundary layers and wakes. One of the first attempts to compute the motion of a single bubble was the seminal work of Ryskin & Leal (1984), who computed the steady-state shape of axisymmetric bubbles. More recently, Takagi & Matsumoto (1994) and Miyata (1996) have conducted three-dimensional simulations of the unsteady motion of deformable bubbles. For systems of many bubbles and particles, the number of published articles is small but growing rapidly. Unverdi & Tryggvason (1992*a*, *b*) computed the interactions of two two- and three-dimensional bubbles; Tomiyama *et al.* (1994) did a computation of four three-dimensional bubbles; Feng, Hu & Joseph (1994, 1995) examined the settling of a few two-dimensional particles in vertical channels; Esmaeeli & Tryggvason (1998) examined the dynamics of two- and three-dimensional systems with a few bubbles at low Reynolds number; Esmaeeli & Tryggvason (1996) studied the energy transfer in a two-dimensional system with a few hundred bubbles at low Reynolds numbers; and Hu (1996) showed the motion of a few hundred two-dimensional solid spheres. Fully three-dimensional simulations of up to a hundred solid spheres have been presented by Johnson & Tezduyar (1997). Here, we continue the studies of Esmaeeli & Tryggvason (1996, 1998) by looking at the behaviour of two- and three-dimensional bubbly flows at moderate Reynolds numbers.

2. Formulation and numerical method

We would like to examine a homogeneous cloud of bubbles rising under the influence of buoyancy. Since it is impractical to model a very large system, we examine the evolution of bubbles in a fully periodic domain. The Navier–Stokes equations govern the fluid motion both inside and outside the bubbles and a single vector equation can be written for the whole flow field. In conservative form it is

$$\frac{\partial \rho \boldsymbol{u}}{\partial t} + \nabla \cdot \rho \boldsymbol{u}\boldsymbol{u} = -\nabla p + (\rho_0 - \rho)\boldsymbol{g} + \nabla \cdot \mu(\nabla \boldsymbol{u} + \nabla \boldsymbol{u}^T) + \sigma \int_F \kappa' \boldsymbol{n}' \delta^\beta(\boldsymbol{x} - \boldsymbol{x}')\mathrm{d}A'. \quad (2.1)$$

Here, $\boldsymbol{u}$ is the velocity, p is the pressure, and ρ and μ are the discontinuous density and viscosity fields, respectively; $\boldsymbol{g}$ is the gravity acceleration and σ is the surface tension coefficient. Surface forces are added at the interface between the bubbles and the ambient fluid. δ^β is a two- or three-dimensional delta function constructed by repeated multiplication of one-dimensional delta functions. The dimension is denoted by $\beta = 2$ or 3. κ is the curvature for two-dimensional flows and twice the mean curvature for three-dimensional flows. $\boldsymbol{n}$ is a unit vector normal to the bubble surface directed into the bubble. Formally, the integral is over the entire front, thereby adding the delta functions together to create a force that is concentrated at the interface. $\boldsymbol{x}$ is the point at which the equation is evaluated and $\boldsymbol{x}'$ is the position of the front. The $\rho_0 \boldsymbol{g}$ term, where $\rho_0 = (1-\alpha)\rho_f + \alpha\rho_b$ is the average density, is added to the equations to prevent uniform downward acceleration of the whole flow field. Here, α is the volume fraction and the subscript f denotes the ambient fluid and b stands for the fluid inside the bubbles. Note that this equation implicitly enforces the proper stress conditions at the fluid interface.

Both the bubbles and the ambient fluid are taken to be incompressible, so the velocity field is divergence free:

$$\nabla \cdot \boldsymbol{u} = 0. \quad (2.2)$$

Equation (2.2), when combined with the momentum equation leads to a non-separable elliptic equation for the pressure. We also have equations of state for the density and the viscosity:

$$\frac{\mathrm{D}\rho}{\mathrm{D}t} = 0, \quad \frac{\mathrm{D}\mu}{\mathrm{D}t} = 0. \tag{2.3}$$

Here, $\mathrm{D}/\mathrm{D}t$ is the material derivative and (2.3) simply states that the density and the viscosity of each fluid remains constant.

Our numerical technique is based on a direct discretization of the 'one-field' formulation, equation (2.1). The basic method is described in Unverdi & Tryggvason (1992*a*) and improvements made in our current implementation are discussed by Esmaeeli & Tryggvason (1998). The method and the code have been tested in various ways as discussed in detail in Esmaeeli & Tryggvason (1998). In this paper we show a grid refinement study. Although mass conservation is not explicitly imposed, in practice mass is well conserved. We have checked the mass conservation in all of our runs and have found that in all cases the maximum error is small, even when the bubbles rise nearly a hundred bubble diameters. In the simulations presented here, we do not allow the bubbles to coalesce. This is done to avoid changes in the system parameters, such as the size and numbers of bubbles, during the simulation. The results show, however, that collisions are relatively rare and this is therefore likely to be a reasonable assumption for the parameter range examined here. In the rare cases when bubbles collide, we make no attempt to resolve the thin layer between the bubbles. While this results in a poor prediction of the layer thickness, a detailed examination of the drainage of a film between two colliding drops (Qian, Tryggvason & Law 1997) showed that the overall collision dynamics was well predicted for drops that did not coalesce, even if the film was not fully resolved.

3. Results

The rise of a single buoyant bubble is governed by four non-dimensional numbers. Two are the ratios of the bubble density and viscosity to the ones of the ambient fluid: $\lambda = \rho_b/\rho_f$ and $\gamma = \mu_b/\mu_f$. The ratios of the material properties are usually small and have little influence on the motion. If we pick the density of the outer fluid, ρ_f, the 'effective' diameter of the bubble, d_e, and the gravity acceleration, g, to make the other variables dimensionless, we obtain

$$N = \frac{\rho^2{}_f d^3{}_e g}{\mu^2{}_f}, \quad Eo = \frac{\rho_f g d^2{}_e}{\sigma}.$$

The first one is a Reynolds number squared based on the velocity scale $(gd_e)^{1/2}$, thus measuring the relative importance of buoyancy and viscous forces. This number is sometimes called the Galileo or the Archimedes number (see Clift, Grace & Weber 1978). The second one is usually called the Eötvös number and is the ratio of buoyancy to surface tension. Often, the Morton number, $M = Eo^3/N^2$, is used instead of N. For multi-bubble flows the volume fraction, α, must also be specified.

In this paper we examine the motion of several buoyant bubbles with $M = 10^{-5}$ ($N = 894.427$) and $Eo = 2$. In terms of a physical system, this Morton number corresponds to a warm motor oil ($\mu_f = 0.0125$ N s m^{-2}, $\rho_f = 880$ kg m^{-3}, $\sigma = 0.03$ N m^{-1}, and $g = 9.81$ m s^{-2}) and the Eötvös number corresponds to a bubble with an effective diameter of about 2.6 mm.† Experimentally it is found that a single air bubble with these parameters in an unconfined domain has a slightly ellipsoidal shape

---

† In Esmaeeli & Tryggvason (1998), the value of μ_f for engine oil was in error. The correct value is 0.0394 N s m^{-2}.

and rises with a Reynolds number of about 31 (figure 2.5 in Clift *et al.* 1978). Here, however, the computations are carried out in two- and three-dimensional domains with fully periodic boundaries, and the finite volume fraction reduces the rise velocity. Although the periodic array is infinite, only one period is computed and as the bubbles originally inside the computed period leave through one boundary, new ones come in through the opposite boundary. While the bubbles in the computed domain interact freely, exactly the same interactions take place in other periods. As the domain size is increased, we hope that the importance of the periodic constraint is reduced. The simplest case is, however, if there is only one bubble in each period. We will refer to this as the 'regular' or 'fixed array' case and use it as a reference to which other results are compared. For dilute bubbly flows where the bubbles rise essentially independently of each other, we expect such a model to capture the dynamics of a many bubble system reasonably well.

When presenting our results, we select d_e, ρ_f, and g as primary independent variables and non-dimensionalize length by d_e and time by $(d_e/g)^{1/2}$. Velocities are scaled by $(d_e g)^{1/2}$ with the exception of the rise velocity of the bubbles, W_b, which is given as a Reynolds number, $Re = \rho_f d_e W_b/\mu_f$. The velocity in units of $(d_e g)^{1/2}$ can be found by dividing the Reynolds number by $N^{1/2}$. The bubble velocities reported here are all the so-called 'drift velocities' (Ishii & Zuber 1979), computed as the difference between the volume-averaged velocities of the bubbles minus the volume-averaged velocity of the whole domain. This corresponds to measuring the bubble velocity with respect to a stationary container where bubbles are injected through the bottom. The liquid has an average velocity given by $W_f = \alpha W_b/(1-\alpha)$ and the relative velocity of the bubbles with respect to the liquid is given by $W_r = W_b/(1-\alpha)$.

3.1. *Resolution test*

Our goal is to shed some light on the behaviour of systems containing many bubbles. Since we suspect that the collective evolution of a large number of bubbles may show a marked difference from a system with a small number of bubbles, we would like to examine as large systems as possible. The motion of each bubble, however, has to be computed accurately and since the computational resources required for our simulations are directly related to the size of our grids, we must find a compromise between the number of grid points required to resolve each bubble and the number of bubbles we simulate. Figure 1 shows a three-dimensional bubble at a steady state and a few streamlines in a reference frame moving with the bubble, computed on a 64^3 grid. The bubble diameter is 0.620 times the size of the periodic domain and therefore we have about 40 grid points per bubble diameter. The results from a 32^3 grid are nearly identical. The rise Reynolds number of the bubble versus time is plotted in figure 2, where we have also added the results from a 32^3 grid and a 16^3 grid. The figure suggests that 20 grid points per bubble diameter (the 32^3 grid) will give adequate resolution. Resolution tests for two-dimensional cases yield similar results and show, in particular, no changes in the solution with further grid refinement. The mass is conserved to within 2.5% after the bubble has risen about twenty diameters for the 32^3 grid and within 1.4% for the 64^3 grid. Resolution tests at other volume fractions, as well as monitoring of the mass conservation for all the results reported in the following sections, yield comparable results.

Another area where we find it convenient to compromise is in the ratio of the material properties of the bubbles and the ambient fluid. Since our study is motivated by the dynamics of gas bubbles in liquids, we would like this ratio to be small

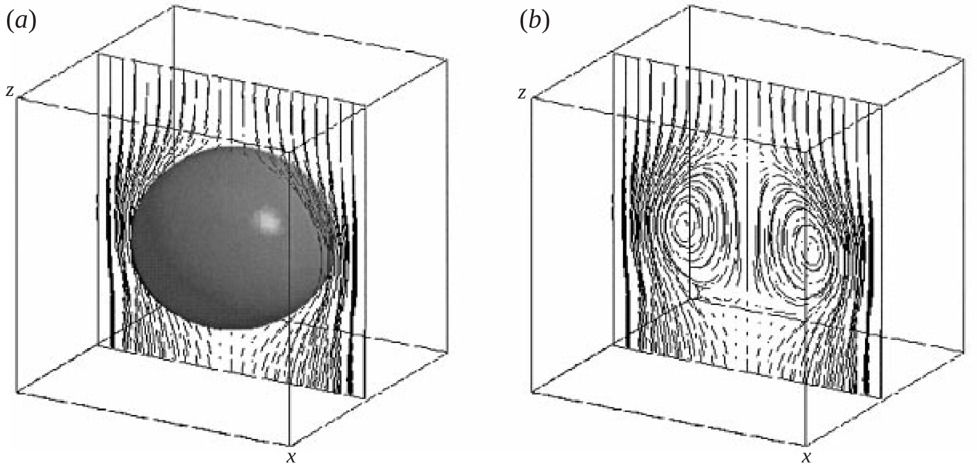

FIGURE 1. The steady-state shape of a rising bubble and the streamlines (*a*) in a frame of reference moving with the bubble computed on a 64^3 grid. Here, $Eo = 2$, $M = 10^{-5}$, $\lambda = 0.1$, $\gamma = 0.1$, and $\alpha = 0.1256$. In (*b*), the bubble has been removed to show the flow inside the bubble.

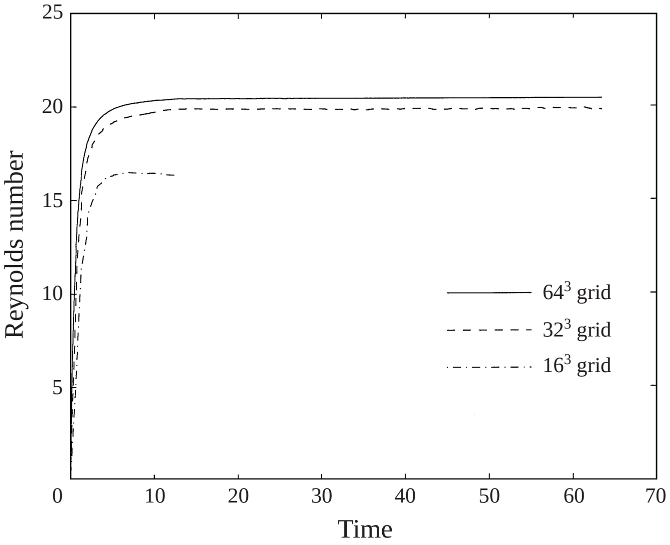

FIGURE 2. The rise Reynolds number as a function of time for three different resolutions, $16^3, 32^3$, and 64^3. Here, $Eo = 2$, $M = 10^{-5}$, $\lambda = 0.1$, $\gamma = 0.1$, and $\alpha = 0.1256$.

(although we note that at high pressures the ratios can be quite large). However, the pressure solver that we use (MUDPACK, see Adams 1989) – which is not optimized to deal with large density jumps – requires many more iterations for small density ratios and occasionally we have experienced difficulties with convergence. While such convergence difficulties can generally be overcome by carefully adjusting the numerical parameters controlling the behaviour of the pressure solver, it is a cumbersome procedure that increases the wall-clock time required for each simulation. We have therefore elected to take the density and viscosity of the bubble to be one tenth that of the liquid in most cases. While this makes the results directly applicable only to somewhat contrived systems (liquid–liquid systems such as oils in liquid metals, for example), we believe that the results yield insight into the behaviour of systems with much smaller ratios of the material properties. Analytical solutions in the Stokes flow limit show that if the viscosity of a buoyant bubble is one tenth that of the ambient fluid the terminal velocity is only reduced by 4.3% from a zero-viscosity bubble. Similarly, a drop that is ten times more viscous than the ambient fluid will fall at a terminal speed that is 3.1% higher than that of a solid sphere. The finite density of the bubble reduces the buoyancy force in direct proportion to its value and also increases the inertia of the bubbles. The added mass coefficient of a spherical bubble is 0.5 and for a cylindrical bubble it is 1.0 and including the finite bubble density results in a maximum difference in the acceleration of about 25% for three-dimensional bubbles and 18% for the two-dimensional ones. In most cases the effect is likely to be smaller, since the bubbles are not exactly spherical (and the added mass is therefore larger) and since the inertia force is small compared to buoyancy and the viscous drag.

We have conducted extensive tests on how the behaviour changes as we change the ratio of the material properties. Esmaeeli (1995) compared the rise of a single bubble at low Reynolds number for ratios between 1/5 to 1/300 and found only a weak dependency on the viscosity ratio (particularly at large values). Similarly, Jan (1994) showed that for axisymmetric bubbles with $Eo = 10$ and $M = 10^{-3}$ the differences between ratios of 1/40 and 1/400 were minimal. We note that while the effect of the ratios of material properties is small for bubbles and drops, there are other cases, such as wind generation of waves and aerodynamic breakup of jets and drops where this is certainly not the case. The above conclusion also does not apply when the ratios are of $O(1)$. A similar problem is encountered in boundary integral computations of drops in Stokes flow where the computational effort increases considerably as the viscosity ratio is increased. For simulations of many drops, Zhou & Pozrikidis (1993, 1994) and Loewenberg & Hinch (1996), for example, thus elected to assume equal viscosities for most of their simulations.

3.2. *The evolution of three-dimensional arrays*

Three three-dimensional simulations of the motion of eight buoyant bubbles are shown in figures 3 and 4. The computations are done in a fully periodic cubical domain, resolved by a 64^3 grid. Gravity points downwards and we follow the motion as the bubbles rise through several periods. The initial bubble configuration is a cubic array, perturbed slightly. The bubbles are shown at time zero and a few later times along with their paths. The computed domain and its periodic extensions in the vertical direction are outlined by thin lines. The volume fraction for the run in (*a*) is 0.0654, 0.1256 for (*b*) and 0.1963 for (*c*). The volume fraction is changed by increasing the size of the bubbles and adjusting other parameters such that other non-dimensional numbers remain unchanged. The density and viscosity ratios are 0.05 for the lowest volume fraction simulation and 0.1 for the other two. The first simulation was done early on in our investigation before we realized that the property ratios could be increased even further without affecting the results in any serious way. Since this makes the computations both easier and faster, the two-dimensional simulations in the later sections were done at these higher ratios as well. The three-dimensional simulations are, however, sufficiently expensive so that we elected not to repeat the low volume fraction simulation. The lowest volume fraction simulation was run to time 120 when the bubbles had risen about 90 diameters and the intermediate volume fraction simulation was run to time 110 at which the bubbles had risen nearly 70

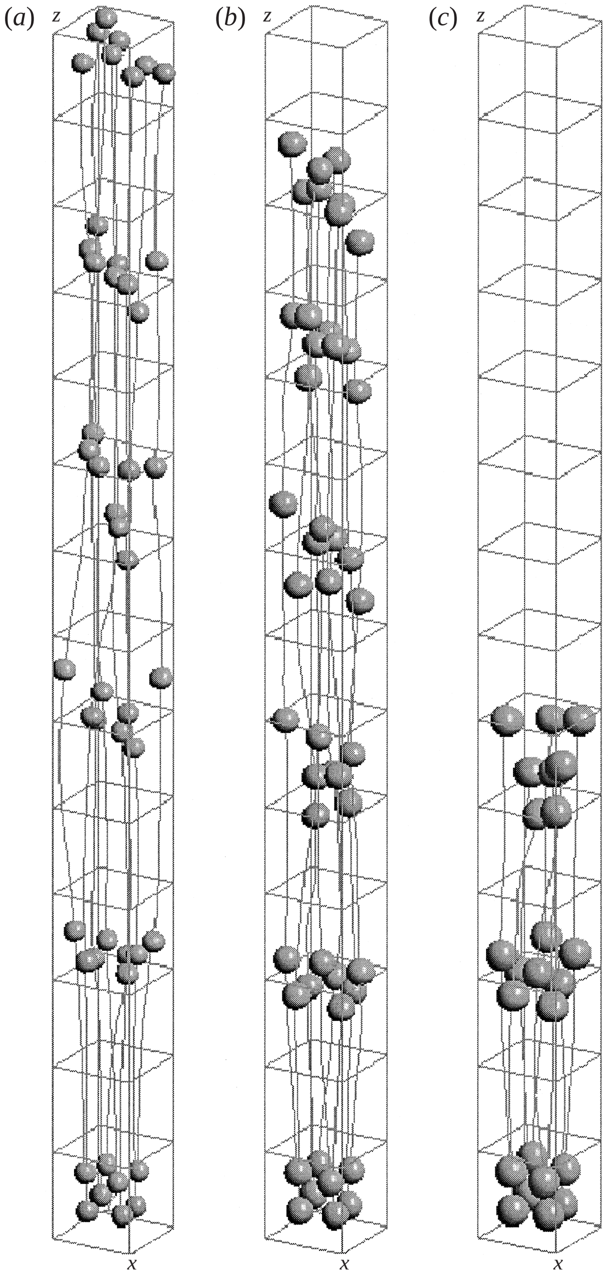

FIGURE 3. The rise of eight three-dimensional bubbles in a periodic domain. The volume fractions are: $\alpha = 0.0654$ (*a*), $\alpha = 0.1256$ (*b*), and $\alpha = 0.1963$ (*c*). The bubbles are plotted at time zero and a few later times along with their paths. The last times plotted are at $t = 70$ for (*a*), $t = 59.6$ for (*b*), and $t = 26$ for (*c*).

diameters. Mass was conserved to within 1.7% for the lowest volume fraction case, within 2.8% for the intermediate volume fraction run, and 1.6% for the highest volume fraction run. Due to difficulty in maintaining mass conservation, the highest volume fraction case was only simulated up to time 26. Note that figure 3 does not

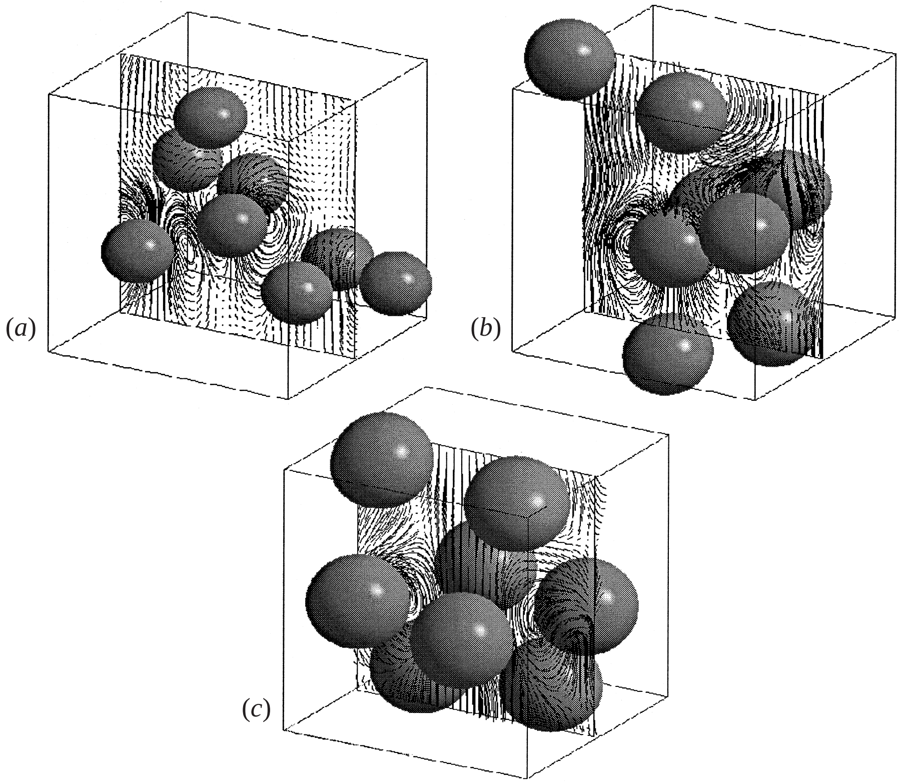

FIGURE 4. The bubbles and the streamlines in the centre-plane at time $t = 70$ for $\alpha = 0.0654$ (*a*), at time $t = 27.3$ for $\alpha = 0.1256$ (*b*), and at time $t = 8.83$ for $\alpha = 0.1963$ (*c*).

show the complete paths up to the final times except for the highest volume fraction case. The $\alpha = 0.1256$ simulation was run for 12 447 time steps and each step took about 60 s on an IBM SP2 workstation. The computational requirements for the other simulations were comparable.

In all three cases the path of each bubble is relatively straight, and although it is obvious that the bubbles have interacted strongly, they have not dispersed much. There is, in particular, nearly no horizontal dispersion. To see the flow induced by the motion, the bubbles and the streamlines in the vertical mid-plane through the computational domain at selected times are plotted in figure 4, for (*a*) $\alpha = 0.0654$ at $t = 70$, (*b*) $\alpha = 0.1256$ at $t = 27.3$, and (*c*) $\alpha = 0.1963$ at $t = 8.83$. The figure shows that the velocity consists of upflow where the bubbles are and downflow in between. There is little horizontal flow and flow structures larger than the bubbles are not visible.

The time evolution of several averaged quantities is shown in figures 5 to 7. The rise Reynolds number, averaged over the eight bubbles is plotted in figure 5. The rise Reynolds number of a completely regular array is also shown (dashed line) as well as the time-averaged value of the average bubble Reynolds number (solid line), defined by

$$\langle Re \rangle = \frac{\rho_f d_e \langle W_b \rangle}{\mu_f},$$

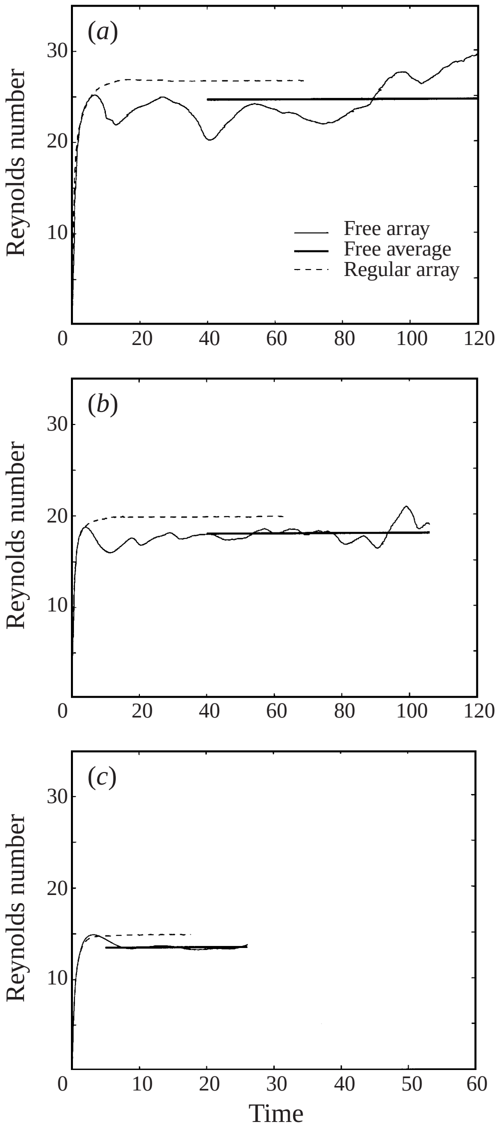

FIGURE 5. The average rise Reynolds number of the bubbles in figures 3 and 4 as a function of time. The result for a regular array at the same volume fraction is also shown. The lengths of the thick lines representing the average Reynolds numbers show the times over which the averaging were done. (*a*) $\alpha = 0.0654$, (*b*) $\alpha = 0.1256$, (*c*) $\alpha = 0.1963$.

where

$$\langle W_b \rangle = \frac{1}{N_b \Delta T} \int_{\Delta T} \sum_{i=1}^{N_b} w_{b_i} \mathrm{d}t. \tag{3.1}$$

Here, N_b is the number of bubbles, ΔT is the time over which the average is taken, and w_{b_i} is the instantaneous vertical velocity of the centroid of bubble i obtained by computing its volume-averaged velocity (see Esmaeeli & Tryggvason 1998 for more detail). The instantaneous velocities of the centroids of the bubbles in the horizontal directions are computed by the same method. The time average is not computed from

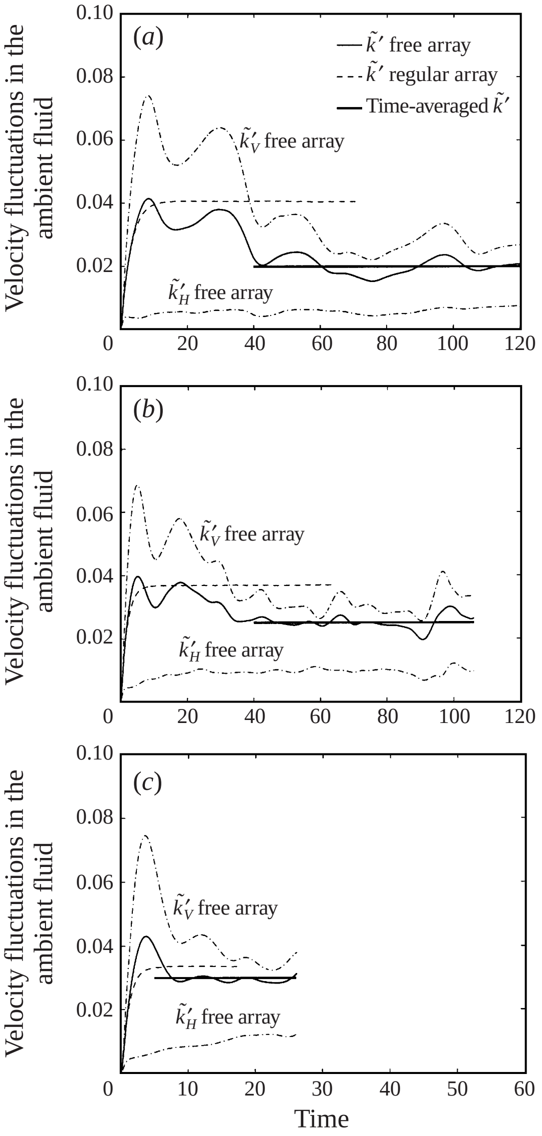

FIGURE 6. The liquid Reynolds stresses and the liquid fluctuation kinetic energy, scaled by $d_e g$, for the bubbles in figures 3 and 4 as a function of time. $\tilde{k}'$ for a regular array at the same volume fraction is also shown. The lengths of the thick lines representing the average fluctuation kinetic energies show the times over which the averaging were done. (*a*) $\alpha = 0.0654$, (*b*) $\alpha = 0.1256$, (*c*) $\alpha = 0.1963$.

time zero, to avoid the initial transient and the length of the solid line represents ΔT. At the earliest time, when the array is still regular, the bubbles approach a rise Reynolds number equal to that of a regular array. As the initially regular array breaks up, the rise Reynolds number decreases. For the lowest volume fraction we see relatively large fluctuations in the average Reynolds number. These fluctuations decrease, both in wavelength and amplitude, as the volume fraction increases. The large increase in the Reynolds number near the end of the lowest volume fraction simulation suggests that in addition to relatively short-time-scale fluctuations, other longer-time-scale variations may also be present. Note that the reduction in the average rise Reynolds number for the freely evolving arrays seen here is exactly opposite to what we found in Esmaeeli & Tryggvason (1998) where freely evolving low Reynolds number bubbles always rose faster than a regular array (in agreement with Stokes flow prediction, see Saffman 1973).

The liquid Reynolds stresses, computed by integrating the velocity fluctuations in the liquid, for all three runs are plotted in figure 6. The vertical component $k'_V = \langle w'w' \rangle$ is plotted separately, but the horizontal components are averaged and we plot $k'_H = \frac{1}{2}(\langle u'u' \rangle + \langle v'v' \rangle)$. In all three cases $\langle u'u' \rangle$ and $\langle v'v' \rangle$ are nearly identical. We also plot the fluctuation kinetic energy, $k' = \frac{1}{2}(\langle u'u' \rangle + \langle v'v' \rangle + \langle w'w' \rangle)$. Both the Reynolds stresses and k' are non-dimensionalized by $d_e g$ and are denoted by $\tilde{k}'_H$, $\tilde{k}'_V$, and $\tilde{k}'$. For all three runs the vertical components are significantly larger than the horizontal ones. The fluctuation kinetic energy is close to that of a regular array initially, but then decays and settles down to a relatively constant value that increases with increasing volume fraction. Since the fluctuation kinetic energy of a regular array decreases slightly with increasing volume fraction, the difference between this quantity for a regular array and a freely evolving one decreases as the volume fraction increases. The lengths of the thick lines show the times over which the averages are taken. The cross-terms, $\langle u'v' \rangle$, $\langle u'w' \rangle$, and $\langle v'w' \rangle$, remain nearly zero and are not plotted here.

Several authors (see Drew & Lahey 1993, for example) have used the potential flow solution for flow over a sphere to model the velocity fluctuations in the liquid. For three-dimensional flows the vertical component is $\langle w'w' \rangle = 4\alpha \langle W_b \rangle^2/20$, the horizontal components are $\langle u'u' \rangle = \langle v'v' \rangle = 3\alpha \langle W_b \rangle^2/20$, and the cross-terms are zero. For two-dimensional flows $\langle u'u' \rangle = \langle v'v' \rangle = \alpha \langle W_b \rangle^2/2$. This results in $k' = \frac{1}{4}\alpha \langle W_b \rangle^2$ for three-dimensional bubbles and $k' = \frac{1}{2}\alpha \langle W_b \rangle^2$ for two-dimensional ones. Here, $\langle W_b \rangle$ is the steady-state rise velocity of a bubble. Although the Reynolds numbers are low here, we have compared the kinetic energy fluctuations with this model. For the kinetic energy we have

$$\frac{k'}{\alpha \langle W_b \rangle^2} = \tilde{k}' \frac{N}{\alpha \langle Re \rangle^2} = 0.25,$$

where $\tilde{k}'$ is the fluctuation kinetic energy non-dimensionalized by $d_e g$ as in figure 6. Using the values for the free arrays in figure 5 and 6, we find that $k'/\alpha \langle W_b \rangle^2 = 0.02N/\alpha \langle Re \rangle^2 = 0.45$ for the lowest volume fraction and slightly higher for the higher volume fractions (see figure 21). The values for the regular array are also higher, presumably because of stronger wake effects compared to the potential flow model. Note also that the difference between the horizontal and the vertical velocity fluctuations is larger than that predicted by the potential flow model. The Reynolds stresses in homogeneous bubbly flows has been measured by Lance & Bataille (1991) who found the horizontal and the vertical components to be of comparable magnitude. Their Reynolds number, however, was much larger than what is used here (a single 5 mm air bubble in water rises at a Reynolds number of about 1000) and their bubbles generally rose along a helical path.

In figure 7, the average velocity fluctuations of the bubbles, defined by

$$K'_H = \frac{1}{N_b} \sum_{i=1}^{N_b} (w_{b_i} - W_b)^2, \tag{3.2}$$

$$K'_V = \frac{1}{N_b} \sum_{i=1}^{N_b} \tfrac{1}{2}((u_{b_i} - U_b)^2 + (v_{b_i} - V_b)^2), \tag{3.3}$$

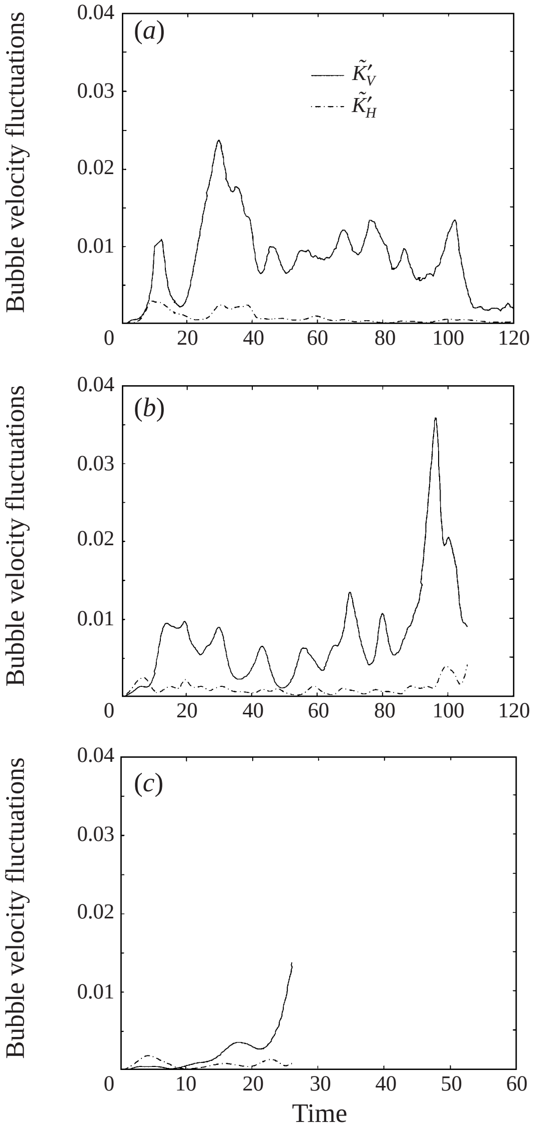

FIGURE 7. The average horizontal and vertical velocity fluctuations of the bubbles in figures 3 and 4 as a function of time. The fluctuations are non-dimensionalized by $d_e g$. (*a*) $\alpha = 0.0654$, (*b*) $\alpha = 0.1256$, (*c*) $\alpha = 0.1963$.

are shown. Here, u_{b_i} and v_{b_i} are the horizontal velocities of the centroid of bubble i and U_b, V_b, and W_b are the instantaneous velocities of the centroid of all the bubbles in the horizontal and vertical directions. In these simulations, U_b and V_b are essentially zero. The fluctuations have been non-dimensionalized by $d_e g$. Note that the velocity fluctuations are not simply the Reynolds stresses of the fluid in the bubbles, since the recirculation inside each bubble is not included. We have also examined the full Reynolds stresses and generally found that the recirculation is well correlated with the average rise velocity. While fluctuations in the bubbles velocity have a strong influence on the motion of the continuous phase, the recirculation is of much smaller importance since the density of the bubbles is small. In all cases the vertical fluctuations are much larger than the horizontal ones. The fluctuations are still undergoing large changes and we have not computed the time averages since the large ‘humps’ in the values near the ends of the $\alpha = 0.1256$ and $\alpha = 0.1963$ runs make the convergence of such averages questionable. Note that the fluctuations have dropped to nearly zero at the end of the low volume fraction run ($\alpha = 0.0654$), indicating that the bubbles are all rising together. The potential flow models of Sangani & Didwania (1993) and Smereka (1993) predict that the bubble rise velocities all become equal and the bubbles form horizontal ‘rafts’. In this case, however, an examination of the bubbles near the end of the run does not show any ‘rafting’ and indeed the velocities increase, confirming the absence of horizontal pairs. We therefore believe that the decrease in the velocity fluctuations is simply a transient effect and that the velocity fluctuations will increase again.

Information about the microstructure of the bubble distribution can be obtained by examining the pair distribution function

$$G(\boldsymbol{r}) = \frac{V}{N_b(N_b-1)}\left\langle \sum_{i=1}^{N_b} \sum_{\substack{j=1 \\ j\neq i}}^{N_b} \delta(\boldsymbol{r}-\boldsymbol{r}_{ij}) \right\rangle . \qquad (3.4)$$

Here, $\boldsymbol{r}$ is a distance vector from the centroid of the reference bubble and $\boldsymbol{r}_{ij} = \boldsymbol{r}_i - \boldsymbol{r}_j$ is the distance vector between the centroids of bubble i and bubble j. V is the total volume of the system. G is obviously not a smooth function and sometimes the Fourier transform of G, the so-called structure function, is used instead (see e.g. Ladd 1993). Examination of the low-wavenumber modes then yields information about the distribution of the delta functions. Here, we take a somewhat more elementary approach and in figure 8 we simply mark the (r, θ) position of each point where the delta function is non-zero for 26, 26, and 16 evenly spaced time intervals (excluding $t = 0$) for $\alpha = 0.0654$ (*a*), 0.1256 (*b*), and 0.1963 (*c*), respectively; r is the distance from the reference bubble and θ is the angle between $\boldsymbol{r}_{ij}$ and the vertical axis. For reference, circles spaced one radius apart mark the distances from the origin and radial lines $\pi/6$ radians apart show the angles with reference to the vertical axis. Since the computed domain is a periodic cube, we only examine bubbles that are located within half the cube dimension from the reference bubble. The dashed circles in (*b*) and (*c*) mark these regions. If the bubbles remain completely spherical, no bubble centre could lie within the second circle.

Although these plots are perhaps somewhat difficult to interpret, two observations stand out. First is the fact that there are very few bubbles directly ahead of (and behind) the reference bubble. This must, however, be interpreted with some care since we do not distinguish between the angular coordinates of the bubble positions, so as we move away from the reference bubble the volume becomes larger and we expect to find more bubbles at larger radial coordinates. The second observation is that for the lowest volume fraction there are no bubbles touching the reference bubble and for the higher volume fractions touching appears to be rather rare. This is as we would expect: two bubbles in a side-by-side position repel each other at finite Reynolds number if they are close enough (but attract weakly if separated further) and at the lowest volume fraction they have the space to do so (see Kim, Elghobashi & Sirignano 1993; Legendre & Magnaudet 1998).

To examine the close interactions in more detail, we have computed the weighted average of G versus time for the interval $d_e < r < 1.75d_e$ for $\alpha = 0.0654$; $d_e < r < 1.5d_e$ for $\alpha = 0.1256$; and $d_e < r < 1.25d_e$ for $\alpha = 0.1963$. Different radial extents of the

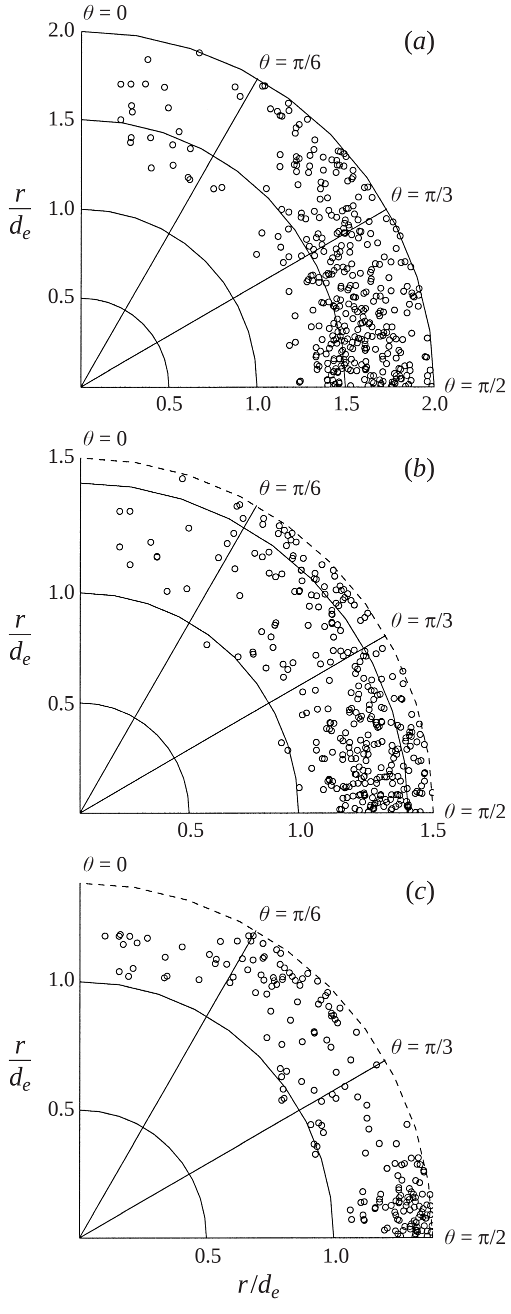

FIGURE 8. The relative positions of the bubbles with respect to a bubble at the origin (open circles). The data are obtained at 26 equispaced times (excluding time zero) for (*a*) $\alpha = 0.0654$ and (*b*) $\alpha = 0.1256$, and at 16 equispaced times for (*c*) $\alpha = 0.1963$. The first and last times are $t = 0.38$ and $t = 118.7$ for (*a*), $t = 0.24$ and $t = 105.9$ for (*b*), and $t = 0.18$ and $t = 26.0$ for (*c*).

integration volume are selected to avoid the periodic boundaries. The weighted average is defined by

$$A = \frac{1}{V}\int G(\boldsymbol{r})P_2^0(\cos\theta)\mathrm{d}v, \tag{3.5}$$

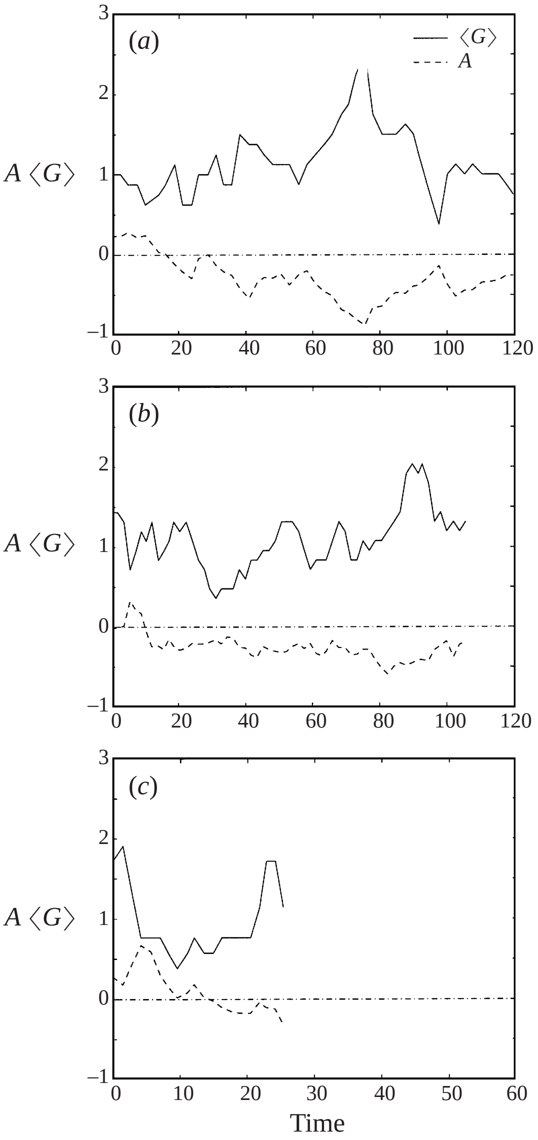

FIGURE 9. The weighted average of G, A, in a shell close to the reference bubble and the average G, $\langle G\rangle$, versus time. Data are obtained at 49 equispaced times for (*a*) $\alpha = 0.0654$, at 61 equispaced times for (*b*) $\alpha = 0.1256$, and at 20 equispaced times for (*c*) $\alpha = 0.1963$.

where $P_2^0 = 3\cos^2\theta - 1$ is the second Legendre polynomial (Ladd 1997). We have also computed the average of G for the same region by

$$\langle G\rangle = \frac{1}{V}\int G(\boldsymbol{r})\mathrm{d}v. \tag{3.6}$$

Figure 9 shows A and $\langle G\rangle$ versus time for the three runs. Initially there are bubbles located within the shell that we are looking at and therefore the lines do not start from zero. $\langle G\rangle$ fluctuates around unity as we expect, since we are examining a relatively large part of the computed domain, but A becomes clearly negative as time increases, indicating a preference for horizontally oriented bubble pairs. This supports the observation made about figure 8 that there are relatively few bubbles located directly behind (and ahead of) the reference bubble. The lack of bubbles on the symmetry axis lends some support to the argument of Koch (1993) who predicted that bubbles would be expelled out of the wake of other bubbles at moderate Reynolds numbers. This hypothesis was important for his subsequent argument that the variance of the bubble velocity remained finite due to screening. The lack of bubbles in the wake is possibly only true for nearly spherical bubbles, since it is well known that axisymmetric deformable bubbles oriented in tandem will attract each other. Spherical or nearly spherical bubbles, however, do not attract each other as strongly and inviscid spherical bubbles actually repel each other (Yuan & Prosperetti 1994). Furthermore, a tandem orientation of two spherical bubbles is an unstable configuration, and a bubble approaching another one will be pushed to the side before collision. Note that vorticity generation which is responsible for both the wake effects and the repulsion of horizontally oriented bubbles when the separation distance is small is completely absent in the potential flow models of Sangani & Didwania (1993) and Smereka (1993). The lack of these effects is likely to be the reason for the strong ‘rafting’ seen in those simulations.

3.3. *The evolution of two-dimensional arrays*

The large computer time needed for the three-dimensional simulations in the preceding section makes it, as yet, impractical to simulate much larger systems. In order to examine what happens when the size of the system is increased and the flow is allowed to evolve for a longer time, we have done several two-dimensional simulations. Two-dimensionality not only reduces the computational cost substantially, but also allows us to obtain a statistically steady state more easily, since the bubble interactions are stronger than in three dimensions.

In figures 10 and 11 the evolution of an initially nearly regular array of sixteen bubbles rising due to buoyancy is shown. The paths of the bubbles are plotted in figure 10. The bubbles initially rise straight up. The initially regular array is unstable, however, and after having moved about one computational domain (ten bubble diameters), it breaks up. As the bubbles rise, their paths often show a rapid change of direction as a result of close interactions of the bubbles. At the end of the simulation, the bubbles are spread out over about five periods vertically, but considerably less horizontally, showing that horizontal dispersion is much smaller than vertical dispersion. Even though the volume fraction for this simulation is the same as that in figure 3(*b*), the paths of the two-dimensional bubbles show much greater fluctuations than the three-dimensional ones due to the much stronger interactions of the two-dimensional bubbles. The bubble shapes and twenty evenly spaced streamlines in a fixed reference frame are plotted at twenty equispaced times in figure 11, starting with the initial conditions in the top left corner. Time increases to the right and down. Unlike the three-dimensional plots in figures 3 and 4, where we followed the bubbles as they moved through different periods, here we plot the bubbles occupying the original period at any given time. The initial array has been perturbed slightly and one row of the bubbles is coloured black to make it easier to follow the motion. The bubble centres are initially placed 2.5 diameters apart, resulting in a volume fraction of $\alpha = 0.1256$. A 256^2 grid is used, resulting in about 25 grid points per bubble diameter. Based on the results from figures 1 and 2, and similar two-dimensional resolution tests, we expect this grid to provide sufficient resolution. Initially, as the bubble array rises, it retains its configuration, but in the third and the fourth frames the array is breaking up rapidly. The motion after the array has

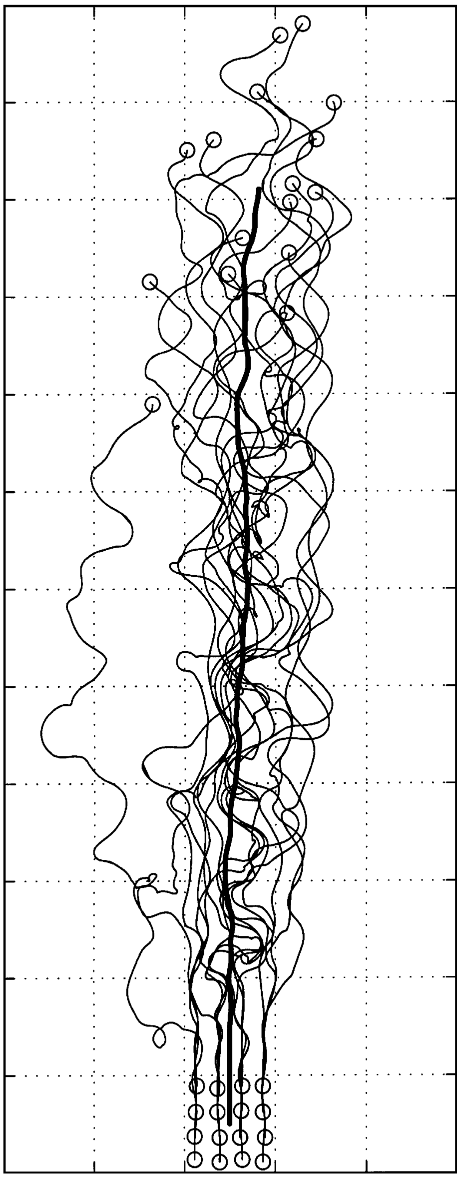

FIGURE 10. The paths of sixteen two-dimensional bubbles. The thick line denotes the centroid. Notice that the size of the circles marking the initial and the final position of each bubble is not to scale.

completely broken up is rather chaotic. However, we can identify one or two large vortices in most of the frames, and we generally find several bubbles moving upward at the edges of these vortices, creating a strong upflow current. In these currents we often see bubbles move upward together. Bubbles that touch are, however, rare. The vortices seen here are relatively weak and are generated by the bubbles moving upward. Therefore, we do not expect to see bubbles forced into the vortex centres, as would happen if the vortices were stronger. Because there is no net upward motion of the liquid, the strong upward currents have to be balanced by downflow. Since there are fewer bubbles there, the downflow is generally much weaker than the upflow. In

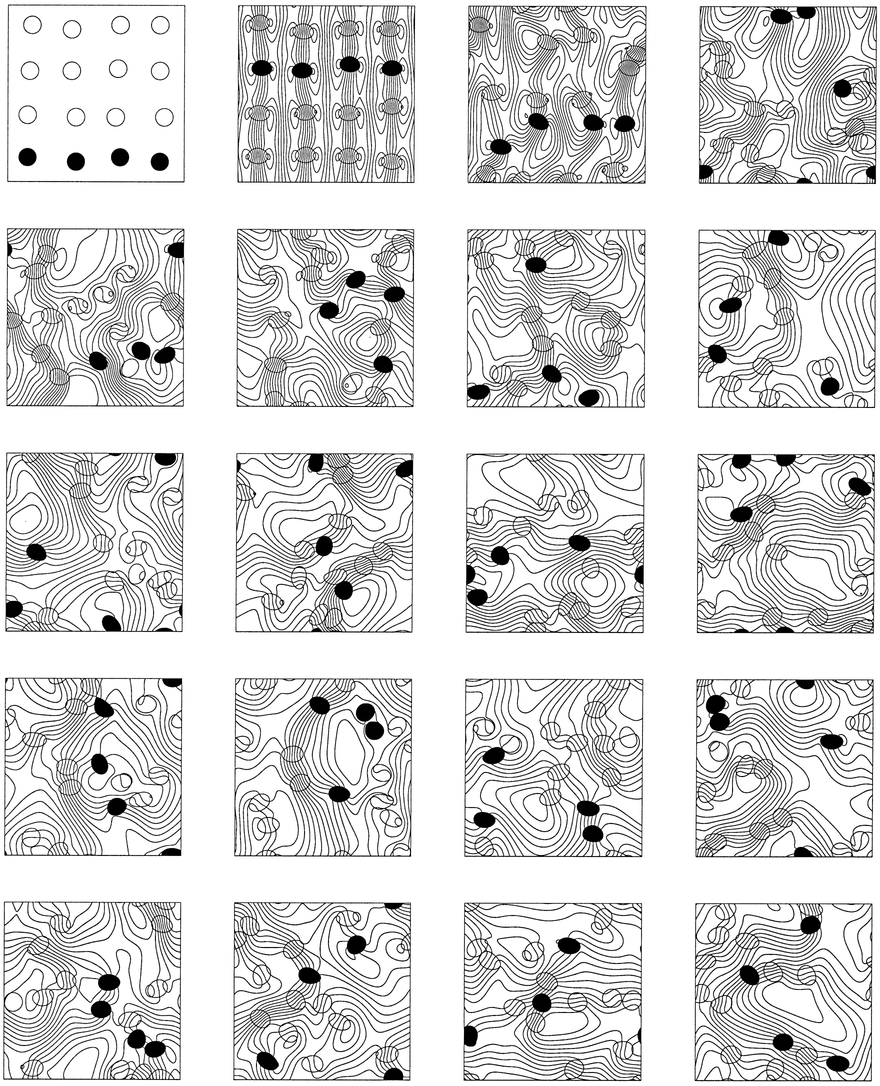

Figure 11. The unsteady rise of sixteen bubbles. The bubbles and the stream function in a stationary frame of reference are shown at twenty equispaced times. The initial positions of the bubbles are shown in the top left-hand corner frame and time increases to the right and down. The final time is $t = 150.2$. One row of the bubbles is coloured black.

several frames we also see strong horizontal flow. Neither the large-scale vortices nor the horizontal motion was seen in figure 4 for the three-dimensional flows, possibly due to the smaller size of the system.

In figures 12 and 13 we show the time evolution of several of the integrated or space-averaged quantities for this flow. The bubble Reynolds number, averaged over the sixteen bubbles is plotted in figure 12. Two horizontal lines, one representing the steady rise Reynolds number of a completely regular array and another one showing the time-averaged value of the average bubble Reynolds number, are also included. The time average is computed from time 30.0 to the end of the run in order to exclude the initial transient. At the earliest time, while the array is still regular, the bubbles approach a rise Reynolds number equal to that

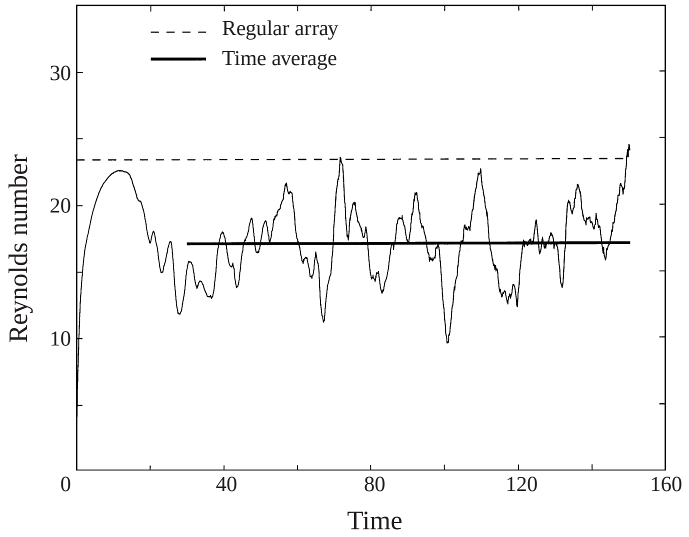

FIGURE 12. The average bubble rise Reynolds number for the simulation in figures 10 and 11. The steady-state value for a regular array with the same volume fraction is shown by a dashed line and the solid horizontal line shows the time average for the free array. The length of the line shows the time over which the averaging was done.

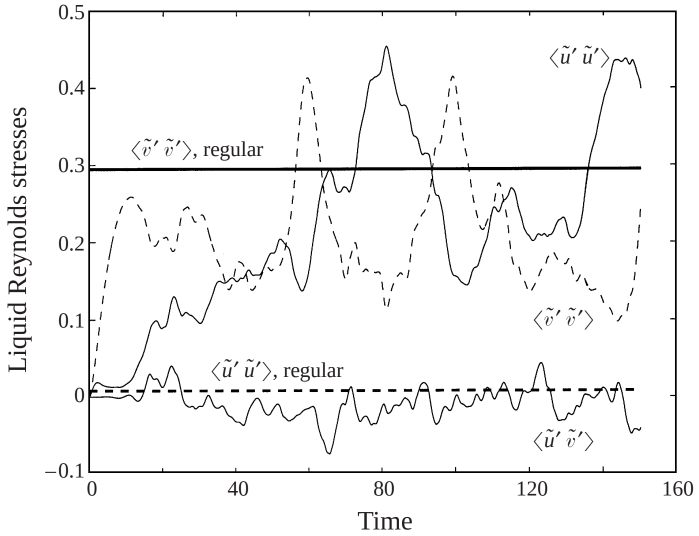

FIGURE 13. The liquid Reynolds stresses ($\langle\tilde{u}'\tilde{u}'\rangle$, $\langle\tilde{u}'\tilde{v}'\rangle$, and $\langle\tilde{v}'\tilde{v}'\rangle$) for the bubbles in figures 10 and 11 as a function of time. The thick dashed and solid lines show the horizontal and vertical Reynolds stresses for a regular array, respectively. The Reynolds stresses are non-dimensionalized by $d_e g$.

of a regular array ($Re = 23.4$ for this volume fraction). As the initial configuration breaks up, the Reynolds number first decreases sharply, and then settles into an irregular and oscillatory pattern, with a mean that is obviously substantially lower than what we find for a regular array. While the general trend is in agreement with the three-dimensional results (and therefore opposite to what Esmaeeli & Tryggvason 1998 found for freely evolving low Reynolds number bubbles) the fluctu-

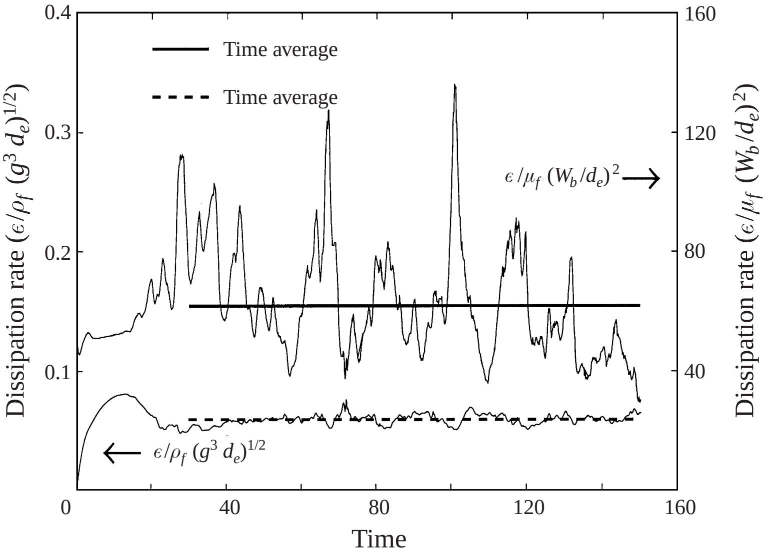

FIGURE 14. The dissipation rate versus time for the simulation in figures 10 and 11. The thick horizontal lines show the time averages for the free array. The lengths of the lines show the times over which the averaging was done.

ations are much larger. Note that the fluctuations contain both relatively short waves (about 5 non-dimensional time units) and longer waves.

The Reynolds stresses for the liquid are plotted versus time in figure 13. As we saw for the three-dimensional case, the vertical component is much larger initially, while the array is still regular, but unlike the three-dimensional results, both components are of comparable magnitudes once the array breaks up. Consequently, the fluctuation kinetic energy is larger for the freely evolving array than for the regular one in the two-dimensional case, whereas it was smaller for the three-dimensional simulations. The cross-term, $\langle u'v'\rangle$, remains nearly zero, as it should. For a two-dimensional flow, the potential flow model (of § 3.2) predicts that

$$\frac{k'}{\alpha\langle W_b\rangle^2} = \tilde{k}'\frac{N}{\alpha\langle Re\rangle^2} = 0.5.$$

Using the data from figure 13, we find that the time-averaged fluctuation kinetic energy is $\tilde{k}' = 0.215$. This yields $k'/\alpha\langle W_b\rangle^2 = 0.215N/\alpha\langle Re\rangle^2 = 5.24$. This large difference will be examined further in the next section.

While the fluctuation kinetic energy of the liquid and the bubbles give information about the magnitude of the perturbations, they contain no information about the spatial scales of the motion. In modelling of single-phase turbulent flows, the turbulent kinetic energy is usually supplemented by the fluctuation energy dissipation to provide such information. To explain why a freely evolving array moves slower than a regular one, we have computed the average dissipation rate by

$$\epsilon = \frac{1}{S}\frac{1}{2}\int \mu \sum_{ij}\left(\frac{\partial u_i}{\partial x_j} + \frac{\partial u_j}{\partial x_i}\right)^2 \mathrm{d}a, \tag{3.7}$$

where the integration is over the whole domain and S is the total area for the two-dimensional simulations. In figure 14 we plot the dissipation rate versus time. The lower curve is $\tilde{\epsilon} = \epsilon/\rho_f(g^3 d_e)^{1/2}$, where $\tilde{\epsilon}$ is the non-dimensional dissipation based on the non-dimensionalization used earlier. The dissipation rate is high initially but then levels off to a somewhat smaller average value, showing that the dissipation decreases when the bubbles slow down, as we would expect. For linear flows (Stokes flow and potential flow) the velocity gradients are proportional to the bubble velocity so dissipation must be proportional to the bubble velocity squared. Assuming that the same is true here, we have also non-dimensionalized ϵ by $\mu_f({W^2}_b/d_e)$, where W_b is the instantaneous velocity of the centroid of the sixteen bubbles. The top curve in the figure shows the non-dimensional dissipation using W_b as velocity scale. The solid horizontal line is its time average. The plot shows that the dissipation rate early on, while the array is still regular, is about 20% lower than the average after the array starts to move irregularly. Thus, the increased dissipation when the bubbles move freely is the reason for the lower rise velocity. We believe that the increased dissipation for the freely evolving finite Reynolds number array is due to a relatively larger amount of vorticity deposited by the unsteady bubble motion. To examine that, we have computed the integral of the vorticity squared (enstropy) in the continuous phase and found that the enstropy divided by the square of time-averaged velocity is larger (by about 25%) in the freely evolving array. Since dissipation is proportional to the vorticity squared (plus terms proportional to the motion of the boundary) this increase slows down the bubbles. We note that a similar phenomenon is also seen for deformable bubbles at higher Reynolds number which slow down if they start to ‘wobble’. Although we believe that the unsteadiness of the motion is an important factor in increasing the net vorticity deposition, we note that Koch & Ladd (1997) found that irregularly positioned circular cylinders had a larger drag compared to a regular array of cylinders.

The average dissipation rate can also be estimated from the bubble rise Reynolds number. At steady state, the rate of work done by the bubbles on the fluid must be balanced by the dissipation rate. This balance can be derived from equation (2.1) which shows, after dropping terms that are identically zero, that

$$\epsilon = \frac{1}{S}\int(\rho_0 - \rho)\boldsymbol{u}\cdot\boldsymbol{g}\,\mathrm{d}a \tag{3.8}$$

at steady state. After carrying out the integration, using the definition of the volume fraction, and that the net momentum flux is zero, we find that the non-dimensional dissipation rate is

$$\tilde{\epsilon} = \frac{\alpha Re}{N^{1/2}}((1-\alpha+\alpha\lambda)(1-\lambda)). \tag{3.9}$$

Using the average Reynolds number from figure 12, we obtain $\tilde{\epsilon} = 0.058$, which is about 2% lower than the average (dashed horizontal line) in figure 14.

Although we believe that the three-dimensional simulations in § 3.2 have reached a statistically steady state, the time over which we followed the motion is not very long and the uncertainty of the various time-averaged quantities therefore is relatively large. The two-dimensional simulations have been carried out for a longer non-dimensional time, but the fluctuations are still large and we anticipate the need to average over a long time to obtain fully converged time averages. To examine how well the time-averaged quantities have converged, we have conducted two additional simulations for the parameters used in figures 10 and 11 but with different initial positions of the bubbles. The results are similar to that of figures 10 and 11 after the

Case no.	Grid size	Re	$\langle\tilde{u}'\tilde{u}'\rangle_l$	$\langle\tilde{u}'\tilde{v}'\rangle_l$	$\langle\tilde{v}'\tilde{v}'\rangle_l$
1	256^2	16.092	0.1612	−0.0014	0.1665
2	256^2	16.368	0.2005	0.0009	0.2092
3	256^2	16.807	0.2465	−0.0112	0.2181

TABLE 1. Time-averaged Reynolds numbers and Reynolds stresses of for sixteen bubbles with three different initial positions. For cases 1 and 2 we used two irregular distributions of bubbles as initial conditions. For case 3 a weakly perturbed regular array was used.

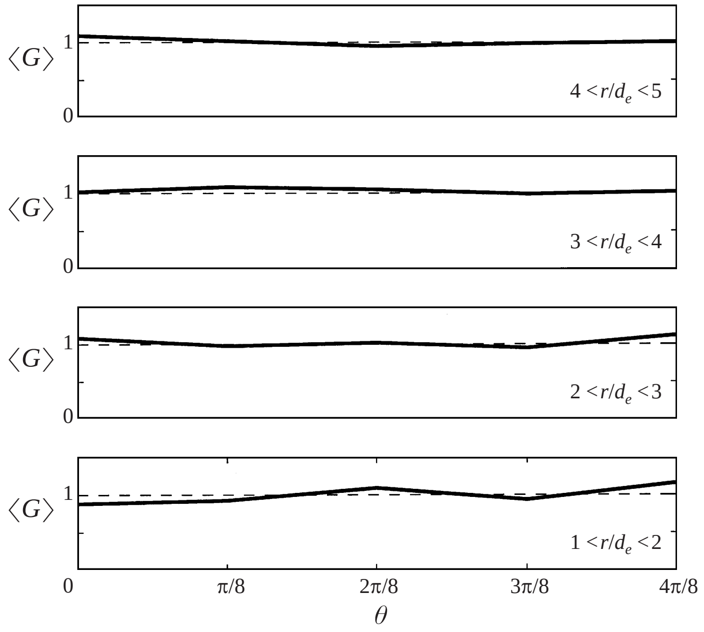

FIGURE 15. The bubble pair distribution function for sixteen bubbles in a periodic cell, computed by averaging the results from three simulations at eighteen equispaced times. $\langle G\rangle$ is shown versus θ for four intervals of $\Delta r = d_e$.

array breaks up, although the detailed evolution of each run is very different. While the time-averaged quantities for each run are not identical, they are relatively close, see table 1.

The larger number of longer runs with more bubbles for the two-dimensional case allows us to get a more complete picture of the pair distribution function compared to the three-dimensional ones. We have computed the pair distribution function for eighteen equispaced times for the three sixteen-bubble runs. The average G is computed over small increments of θ, the angle between $\boldsymbol{r}_{ij}$ and the vertical axis, and over small increments of r, the distance from the reference bubble. In figure 15 we plot $\langle G(\theta)\rangle_{\Delta r}$ for four intervals between $r/d_e = 1$ and 5. Here, $\Delta\theta = \pi/8$ and $\Delta r = d_e$. The plot shows that for the first interval, $\langle G(\theta)\rangle_{\Delta r}$ has a very small maximum for $\theta = \pi/2$ and a very small minimum for $\theta = 0$, but at larger radii, $\langle G(\theta)\rangle_{\Delta r}$ is essentially constant. To condense these information even further, we have also computed the

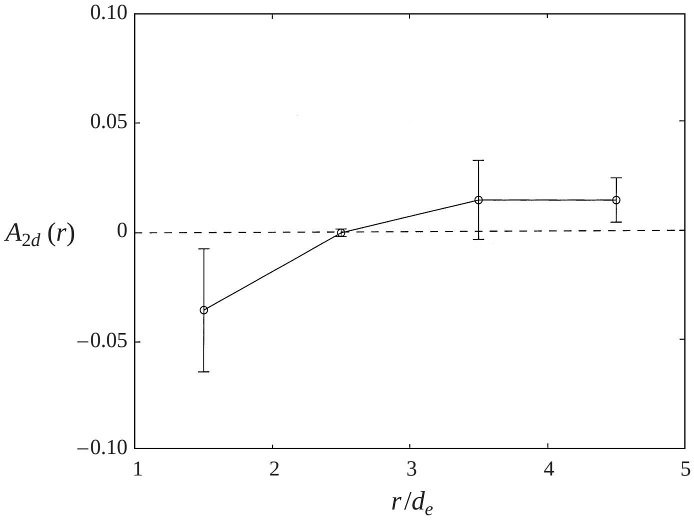

FIGURE 16. The weighted average of the bubble pair distribution function, $A_{2d}(r)$, versus non-dimensional radius, averaged over three runs at eighteen equispaced times. The standard deviations of the averages are shown by vertical error bars.

weighted average of G by

$$A_{2d}(r) = \int_{\Delta r} \int_0^{2\pi} G(r, \theta) \cos 2\theta \mathrm{d}a. \tag{3.10}$$

A negative value of A_{2d} indicates a preference for a horizontal alignment of the bubbles and if the bubble distribution is isotropic, $A_{2d} = 0$. In figure 16 we plot this quantity for the same increments in r as used in figure 15. For $r < d_e$, A_{2d} is not defined since there are no bubbles there. For $d_e < r < 2d_e$, A_{2d} is negative but a small positive value is found for the other radii. The uncertainty is, however, large and we expect $A_{2d}(r)$ to approach zero as r becomes larger. The relatively uniform distribution of bubbles found here is clearly opposite to what is found for the three-dimensional bubbles where there was a clear preference for a side-by-side orientation. Comparison of these results with comparable quantities at lower Reynolds numbers in Esmaeeli & Tryggvason (1998) reveals that the three-dimensional bubbles show an increased tendency toward a side-by-side orientation as the Reynolds number is increased, but the two-dimensional results show the opposite trend.

3.4. *Decomposition of the two-dimensional Reynolds stresses*

When bubbles move through a quiescent liquid, their motion causes velocity fluctuations in the liquid even though turbulent motion due to vorticity is absent. These velocity fluctuations lead to Reynolds stress terms in the averaged two-fluid equations and are usually referred to as ‘pseudo’ turbulence. In addition, the bubbles can generate unsteady vorticity that causes ‘real’ turbulence. The velocity fluctuations plotted in figure 6 and 13 are the total velocity fluctuations. A number of authors have modelled the velocity fluctuations due to the bubble motion (the ‘pseudo’ turbulence) by using the velocity field of an isolated spherical bubble moving in a potential flow. If the Reynolds number is sufficiently high, and the volume fraction and the Eötvös number are low, this model can be expected to give a reasonable estimate for the velocity fluctuations.

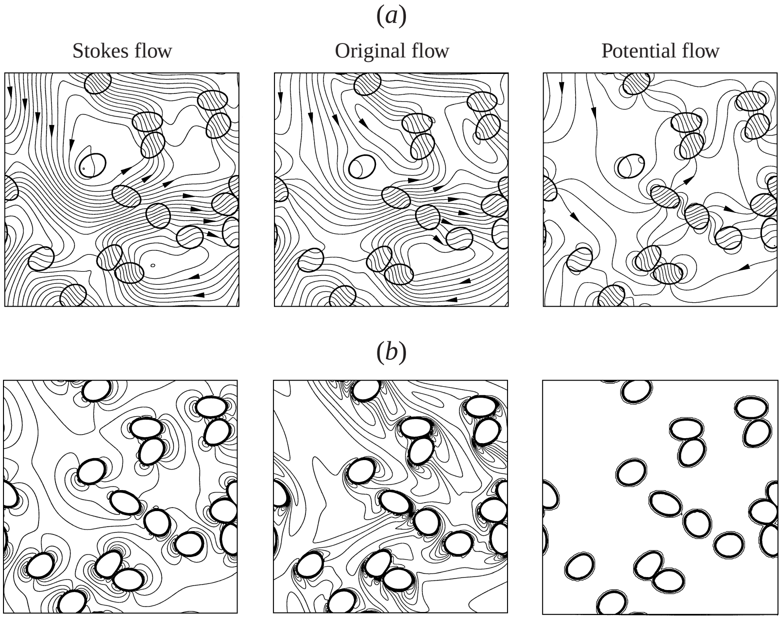

FIGURE 17. (*a*) The stream function and (*b*) the vorticity field at time 75.9 for the simulation in figures 10 and 11 (middle frame) along with the stream function computed by assuming Stokes flow (left frame) and potential flow (right frame) and the same bubble velocities.

Although it is perhaps somewhat surprising that the fluctuation kinetic energy for the three-dimensional simulations is of the same order as the predictions of the potential flow model (the Reynolds number is, after all, not very high here), the large difference between the potential flow and the two-dimensional results is even more unexpected. In order to examine the two-dimensional results in more detail, we have computed the potential flow around the two-dimensional bubbles at a few times and compared the 'pseudo' turbulence with the total Reynolds stresses. Before we present the results, we describe briefly how we do this in the context of the 'one-field' formulation. The fundamental idea is that the surface of the bubble is a vortex sheet, separating the flow inside the bubble (which is not necessarily irrotational) and the ambient potential flow. We find the strength of the vortex sheet (which is represented on the fixed grid as a region of concentrated vorticity) iteratively. First we set the velocity outside the bubble equal to zero, leaving the velocity inside the bubble unchanged. Then we numerically differentiate the velocity to find the vorticity (which is non-zero only inside the bubbles and at their boundaries). Given the vorticity we compute the stream function by solving a Poisson equation and find a new velocity field by numerical differentiation. Initially, the velocity inside the bubble computed in this way is different from the original one. We therefore set the velocity inside the bubble to its original value again, leaving the outside velocity unchanged, and repeat the procedure. This iteration is continued until the irrotational velocity field outside the bubble does not change. The process converges relatively fast and we have verified that it produces the correct solution by comparing the result with the flow field due to a periodic array of dipoles. We have also computed the Stokes flow around the bubbles by a similar procedure where we keep the velocity inside the bubbles unchanged but allow vorticity to diffuse so that $\nabla^2\omega = 0$ and $\nabla^2\psi = -\omega$ in the domain outside the bubbles. Again, this iteration converges relatively fast.

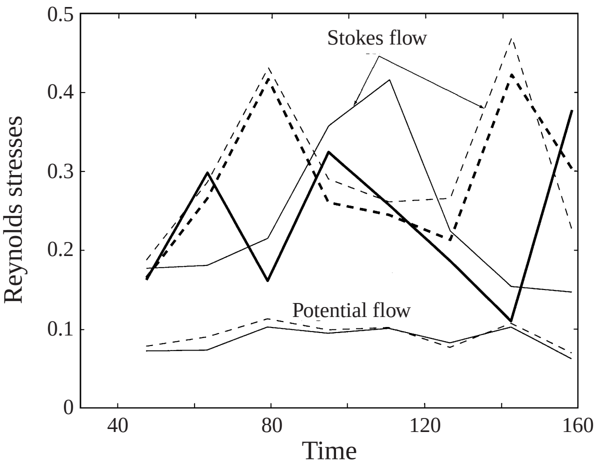

FIGURE 18. Vertical and horizontal Reynolds stresses of the ambient fluid versus time for the original, Stokes, and potential flow. Thick lines represents Reynolds stresses for original flow. The vertical stresses are shown by the solid lines and the horizontal stresses are shown by dashed lines. The Reynolds stresses are non-dimensionalized by $d_e g$.

In figure 17(*a*) the streamlines at time 75.9 from the computations in figures 10 and 11 (centre) are compared to the streamlines of a potential flow (right) and a Stokes flow (left) computed in the way described above. Although the bubble velocities are the same, the potential flow has relatively little in common with the original velocity field. The velocity outside the bubbles is generally much smaller and the strong ‘streams’ seen in the original field are nearly absent. The Stokes flow shows much stronger similarities, although several differences are immediately noticeable. The downflow ‘streams’ in the left half of the domain are stronger, and the wake behind the bubbles in the top right corner is absent. The corresponding vorticity fields are shown in figure 17(*b*). For the potential flow the vorticity is bound to the surface of the bubbles as an infinitely thin vortex sheet, but for the Stokes flow the vorticity diffuses sufficiently rapidly away from the bubble surface so that its Laplacian is zero. For intermediate Reynolds numbers the vorticity is both diffused and advected from the bubble surface, resulting in higher vorticity values in the flow outside the bubbles (the integrated enstropy is about 18% higher than that of the Stokes flow). Figure 18 shows the horizontal and vertical Reynolds stresses versus time (computed at seven times only) for the bubble-generated potential flow, the original velocity field (shown by thick lines), and the Stokes flow. The vertical and horizontal Reynolds stresses are shown by solid and dashed lines, respectively. It is clear that the potential flow yields much smaller Reynolds stresses than the finite Reynolds number flow (about one fifth). The Stokes flow field, on the other hand, produces fluctuation kinetic energy that is only slightly higher than that of the original flow. The vertical component of the Reynolds stresses is somewhat higher than the horizontal component for the Stokes flow and the finite Reynolds number one, but the horizontal and vertical components are about equal for the potential flow, as we expect.

3.5. *Effect of system size*

Although the simulations in § 3.3 resulted in relatively well-converged averaged quantities, the question remains whether the results are applicable to systems with an arbitrary number of bubbles. While it seems reasonable to expect that if the largest

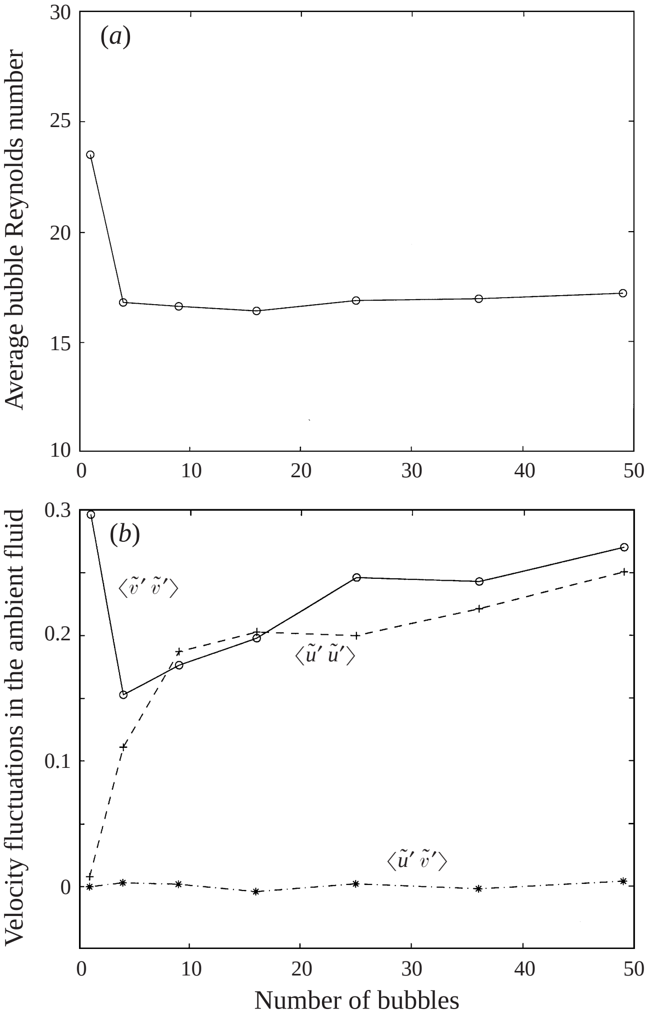

FIGURE 19. (*a*) Average bubble rise Reynolds number versus number of bubbles. The Reynolds numbers are obtained by taking the time average of the instantaneous velocity of the centroid of the bubbles and ensemble average over three simulations with different initial bubbles positions. (*b*) Average velocity fluctuations in the ambient liquid versus number of bubbles. The fluctuations are non-dimensionalized by $d_e g$.

flow scales are much smaller than the dimension of the system, then the evolution would be independent of the system size, we do not know, *a priori*, the sizes of the largest flow scales. This question is particularly relevant for the two-dimensional results, since we have shown in Esmaeeli & Tryggvason (1996) that for low Reynolds number bubbly flows there is an inverse energy cascade that feeds energy to lower wavenumbers in a way similar to what is seen for two-dimensional turbulence. This leads to a continuous growth of the largest flow scales and can prevent the emergence of a statistically steady state. Furthermore, even if the system does reach a steady state, we need to know how large a system needs to be simulated in order to yield averaged quantities that are representative of a truly infinitely large system.

To address this issue, we have computed the evolution of several two-dimensional systems with different numbers of bubbles. The non-dimensional parameters are the same as those in the runs discussed earlier and the grid size has been selected in such a way that the resolution per bubble remains the same. For each system size, we have conducted three simulations, one with a slightly perturbed regular bubble array as initial conditions and the other two starting from more irregular bubble distributions. All the simulations were carried out until non-dimensional time 158. In figure 19 we plot the time-averaged bubble Reynolds number (*a*) and the Reynolds stresses (*b*) versus the number of bubbles in the system. The rise Reynolds number is essentially independent of the number of bubbles but does not approach the one-bubble result smoothly. The Reynolds stresses, on the other hand, increase slightly with the number of bubbles. The largest difference is between one bubble (regular array) and four freely evolving bubbles, showing the importance of the unsteady bubble interactions. Based on the results of Esmaeeli & Tryggvason (1996) for many two-dimensional bubbles at low Reynolds numbers, we believe that the increase in velocity fluctuations is a result of an inverse energy cascade where a fraction of the work done on the liquid by the bubbles goes to increase the energy content of the low-wavenumber modes. If that is the case here, then the evolution of a large three-dimensional system will be different, although flow structures much larger than the bubbles could certainly appear.

3.6. *Effect of volume fraction*

For a homogeneous distribution of equal size bubbles, the volume fraction is the most important controlling parameter and determining how the various properties of the mixture change with volume fraction is of key interest. In addition to the three-dimensional simulations in § 3.2, we have conducted several two-dimensional simulations of sixteen bubbles with different volume fractions. Three simulations were done for each volume fraction. All the simulations were started from similar initial conditions (perturbed regular arrays) and were carried out until an approximately steady state was reached. The grid was adjusted in such a way that the resolution per bubble was the same as in figures 10 and 11.

The average rise Reynolds number is plotted versus volume fraction in figure 20. At low volume fraction the regular two-dimensional arrays rise faster than the two-dimensional freely evolving ones, but the Reynolds numbers of the regular arrays decrease faster than those of the freely evolving arrays and at about $\alpha = 0.3$ the Reynolds numbers are the same. It is perhaps at first surprising to find a large difference between the fixed and the free two-dimensional arrays for low volume fractions. Intuitively, we would expect the difference to approach zero in the limit of $\alpha \rightarrow 0$ (as we found at low Reynolds numbers in Esmaeeli & Tryggvason 1998). We believe that the reason for the apparent divergence as the volume fraction decreases is that the bubbles are still interacting strongly and the unsteady motion causes a larger dissipation than in the steady-state array. As the volume fraction is increased, the ‘mobility’ of the bubbles is reduced and the results are more like what is seen for a regular array. At very low volume fractions, where the bubbles are essentially independent of each other, we would, of course, expect the free array and the fixed one to yield the same rise velocity. We believe, however, that this volume fraction is much lower than what we have simulated so far. The average rise Reynolds numbers for the three-dimensional simulations are also shown in figure 20 along with the results for a regular three-dimensional array at the same volume fractions. Those results show a similar trend to the two-dimensional one, but the difference between a regular array and a freely evolving one is much smaller. Experimental results show considerable reduction in the rise velocity of bubbles as the volume fraction is increased. Ishii & Zuber (1979) summarized a large amount of data for bubbles, drops, and particles

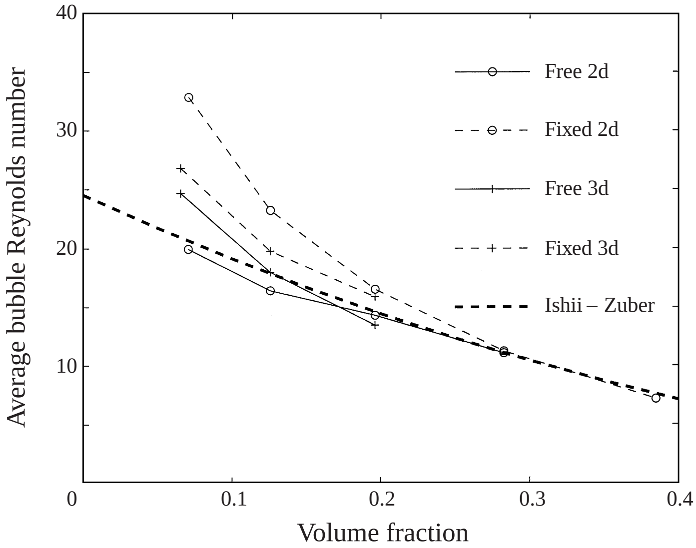

FIGURE 20. The bubble Reynolds number versus volume fraction. The Reynolds numbers for both two- and three-dimensional free arrays are obtained by taking time average of the instantaneous velocity of the centroid. The results for the two-dimensional free arrays are obtained by taking the ensemble average of the time-averaged Reynolds number over three simulations with different initial bubble positions. The Ishii–Zuber (1979) correlation is added for comparison.

and found correlations for the drift velocity in the various flow regimes. For bubbles they identified the 'Stokes regime', where the drift velocity decreased as $(1-\alpha)^3$; the 'undistorted particle regime', where the relationship was slightly more complex; and the 'distorted particle regime', where the drift velocity decreased as $(1-\alpha)^{1.7}$. At higher flow rates, in the 'churn turbulent regime' the drift velocity was found to be independent of the volume fraction. Our results fall in the 'undistorted particle regime' and in figure 20 we include the Ishii–Zuber correlation as a thick dashed line. While the correlation predicts values comparable to the simulated ones, it differs in two aspects. The slope of the experimental curve is smaller and the prediction for $\alpha = 0$ is lower than an extrapolation of the simulated values. The difference at zero volume is most likely due to uncertainties in the correlation. The experimental correlations used by Clift *et al.* (1978) to produce their 'bubble map' (figure 2.5) yields a rise Reynolds number of about 30 or about 18% higher than the Ishii–Zuber correlation. It is also likely that both correlations were based on bubbles where surfactant effects (absent in the simulations) may have played a role. The difference in slope is perhaps more surprising. The results for the two-dimensional bubbles show a large difference between the slope of the Reynolds number versus volume fraction curve for a free and a fixed two-dimensional array due to the large reduction in rise velocity at low volume fraction where the 'mobility' of the bubbles is larger. The fact that the slope is nearly the same for the free and the fixed three-dimensional array suggests that the small number of bubbles may be the reason for the difference with the Ishii–Zuber correlation. Indeed, preliminary computations of a larger system (64 bubbles) with comparable parameters show about twice the reduction found here (Bunner & Tryggvason 1997). Further studies of larger systems should help clarify this issue.

In figure 21, we plot the kinetic energy fluctuations versus volume fraction. Theoretical results based on potential flow theory predict that $k'/\alpha\langle W_b\rangle^2$ is a constant

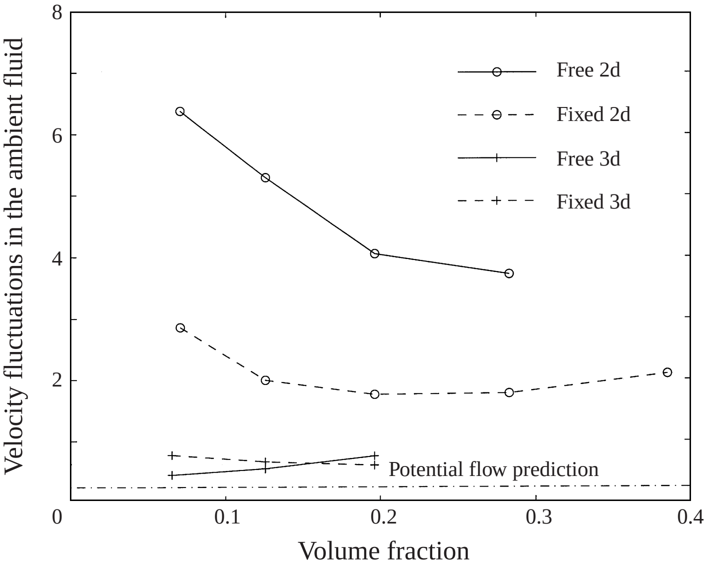

FIGURE 21. The effect of the volume fraction on the average fluctuation kinetic energy, k', of the ambient fluid. Data points for the free arrays are obtained by taking the time average over the instantaneous velocity fluctuations (for both two- and three-dimensional bubbles) and taking the ensemble average over three simulations of two-dimensional bubbles with different initial bubble positions. k' is scaled by $\alpha\langle W_b\rangle^2$, where $\langle W_b\rangle$ is the steady-state rise velocity of the regular arrays and the time-averaged rise velocity of the free arrays.

and in the figure we use this non-dimensionalization. The results show considerable differences between the two- and the three-dimensional cases as we observed earlier. The two-dimensional freely evolving array exhibits strong variations with the volume fraction showing that the 'mobility' of the bubbles and hence the velocity fluctuations are greatly reduced at high volume fractions where the bubbles are more tightly packed. While we expect k' to approach zero as $\alpha \rightarrow 0$ it is clear that if $k' \sim \alpha^n$, then $n < 1$ for both the free and the regular array. The three-dimensional results are, however, much closer to a constant (at least for the range of α examined) and the free array shows a trend opposite to the rest, with $k'/\alpha\langle W_b\rangle^2$ increasing slightly with α, in addition to being smaller compared with the regular array. The values are also much smaller than those of the two-dimensional array and relatively close to what the potential flow model predicts ($k'/\alpha\langle W_b\rangle^2 = 0.25$), particularly for the freely evolving low volume fraction array.

4. Conclusions

We have examined the dynamics of homogeneous two- and three-dimensional finite Reynolds number bubbly flows by direct numerical simulations where inertia, viscosity, and surface tension are fully accounted for. The values of the non-dimensional viscosity (Morton number) and diameter (Eötvös number) were kept fixed, but the number of bubbles and the volume fraction were varied. This study complements an earlier study of a similar system (Esmaeeli & Tryggvason, 1996, 1998) where the Reynolds numbers were much lower (about 1–2, depending on the volume fraction and the dimensionality). Owing to finite computational resources, the three-dimensional simulations have been limited to only eight bubbles per periodic box. We have not, however, made any of the simplifying assumptions common to earlier attempts to simulate multifluid systems, such as potential flow, Stokes flow, or point particles.

The results presented here and in Esmaeeli & Tryggvason (1998) show the following.

(i) A regular array is an unstable configuration that breaks up through interaction between bubbles that are initially in an 'in-line' configuration.

(ii) At moderate Reynolds numbers, $Re \sim 10$–30, freely evolving bubbles rise slower than regular arrays. For low Reynolds numbers, $Re \sim 1$–2, freely evolving arrays rise faster as predicted by theories based on Stokes flow. Our results suggest that the increased deposition of vorticity at finite Reynolds numbers by the unsteady bubble motion and/or the irregular bubble distribution is the reason for the opposite effect at higher Reynolds numbers.

(iii) As the Reynolds number increases, there is an increased trend toward 'side-by-side' configurations of bubble pairs for nearly spherical three-dimensional bubbles. Potential flow computations predict the formation of horizontal layers for bubbles with a comparable rise velocity and it is likely that there is a monotonic increase in the probability of horizontal pairs, from the relatively weak preference seen for Stokes flow to the strong trend observed for potential flows. This effect is not seen for two-dimensional bubbles.

One of the key unanswered questions for the systems simulated here is what happens in three-dimensional systems as the number of bubbles becomes larger. In particular, we would like to know if large flow structures emerge at late times and if the velocity fluctuations diverge with the size of the system. In real flows such as bubble columns and bubbles entrained by breaking waves, for example, geometry, injection, or external flow can lead to large flow structures. Here, such factors are absent and we hope that the results become independent of the size of the system once it is large enough. This may, however, not necessarily be the case. There is mounting evidence that velocity fluctuations for suspension of particles in Stokes flow diverge as the system becomes larger (Ladd 1993, 1997) and we have shown that for two-dimensional low Reynolds number flows there is an inverse energy cascade that continuously feeds energy to the large flow scales in a way similar to what is seen for two-dimensional turbulence. For three-dimensional finite Reynolds bubble flows Koch (1993) has, on the other hand, argued that the wakes of bubbles produce a shielding effect resulting in convergent velocity fluctuations. As yet, we are not in a position to settle this issue. For the two-dimensional simulations we found a weak dependence on the number of bubbles, possibly due to an inverse energy cascade, but for the fully three-dimensional case we do not have enough data to make definite statements about the effect of the system size. Our simulations did, however, show a deficit of bubbles in the wakes of other bubbles as required by the Koch (1993) theory.

While the two-dimensional results were very successful in yielding well converged averages with a relatively modest number of bubbles and in a time that is well within the ranges of current computer power, their usefulness in providing insight into the three-dimensional dynamics was (not surprisingly) somewhat mixed. In general, the two-dimensional results predicted the correct trend. However, the interactions between the bubbles are strongly over-predicted (again not particularly surprising) and even for the same volume fraction the two-dimensional systems showed much larger fluctuations compared to the three-dimensional ones. This difference was particularly striking for the velocity fluctuations in the liquid where the three-dimensional results were of the same order of magnitude as the predictions of a simple potential flow model, but the two-dimensional results were not.

Although we have focused on relatively modest Reynolds numbers so far, there is nothing in our methodology that prevents simulations of much higher values. The key consideration is that the resolution requirement increases with increase in Reynolds number. Since this leads to a much larger number of grid points needed to resolve each bubble at higher Reynolds numbers, the number of bubbles that can be simulated on a given grid is obviously much smaller than for lower Reynolds numbers. Esmaeeli (1995) shows a few two-dimensional simulations of bubbles with Reynolds numbers up to 800. We have also been limited in the present paper to relatively small three-dimensional systems. Again, this is only a matter of the total number of grid points. A parallel version of the code used here should allow an order of magnitude increase in the size of the computations.

This work was supported by the National Science Foundation under grant CTS-9503208. The computations were done on the computers at the San Diego Supercomputer Center, which is sponsored by the NSF, and at the Center for Parallel Computing (CPC) at the University of Michigan. We would like to thank Dr Hal Marshall for his help with using the CPC facilities and Dr John Adams at NCAR for sending us a copy of his latest version of MUDPACK.

REFERENCES

ADAMS, J. 1989 MUDPACK: Multigrid FORTRAN software for the efficient solution of linear elliptic partial differential equations. *Appl. Maths Comput.* **34**, 113–146.

BLAKE, J. R. & TONG, R. P. 1995 Jet impact in collapsing bubbles. *Proc. 12th Australian Fluid Mechanics Conf. Sydney*, pp. 819–822.

BRADY, J. F. 1993 Stokesian dynamics simulation of particulate flows. In *Particulate Two-Phase Flow* (ed. M. C. Roco), pp. 912–950. Butterworth.

BUNNER, B. & TRYGGVASON, G. 1997 Simulations of large bubble systems. *ASME Fluids Engineering Division Summer Meeting, June 22–26.*

CHAHINE, G. L. 1994 Strong interactions bubble/bubble and bubble/flow. In *Proc. IUTAM Conf on Bubble Dynamics and Interfacial Phenomena* (ed. J. R. Blake). Kluwer.

CLIFT, R., GRACE, J. R. & WEBER, M. E. 1978 *Bubbles, Drops, and Particles*. Academic.

CLIMENT, E. & MAGNAUDET, J. 1997 Simulation d́éCoulements induits par des bulles dans un liquide initialement au repos. *C. R. Acad. Sci.* Paris (II b) **324**, 91–98.

DREW, D. A. & LAHEY, R. T. JR. 1993 Analytical modeling of multiphase flow. In *Particulate Two-Phase Flow* (ed. M. C. Roco), pp. 509–566. Butterworth.

ESMAEELI, A. 1995 Numerical simulations of bubbly flows. PhD Thesis, The University of Michigan.

ESMAEELI, A. & TRYGGVASON, G. 1996 An inverse energy cascade in two-dimensional, low Reynolds number bubbly flows. *J. Fluid Mech*, **314**, 315–330.

ESMAEELI, A. & TRYGGVASON, G. 1998 Direct numerical simulations of bubbly flows. Part 1. Low Reynolds number arrays. *J. Fluid Mech*, **377**, 313–345.

FENG, J., HU, H. H. & JOSEPH, D. D. 1994 Direct simulation of initial value problems for the motion of solid bodies in a Newtonian fluid. Part 1. Sedimentation. *J. Fluid Mech.* **261**, 95–134.

FENG, J., HU, H. H. & JOSEPH, D. D. 1995 Direct simulation of initial value problems for the motion of solid bodies in a Newtonian fluid. Part 2. Couette and Poiseuille flows. *J. Fluid Mech.* **277**, 271–301.

HARLOW, F. H. & WELCH, J. E. 1965 Numerical calculation of time-dependent viscous incompressible flow of fluid with free surfaces. *Phys. Fluids* **8**, 2182–2189.

HIRT, C. W. & NICHOLS, B. D. 1981 Volume of fluid (VOF) method for the dynamics of free boundaries. *J. Comput. Phys.* **39**, 201–205.

HU, H. H. 1996 Direct simulation of flows of solid-liquid mixtures. *Intl J. Multiphase Flow* **22**, 335–352.

ISHII, M. & ZUBER, N. 1979 Drag coefficient and relative velocity in bubbly, droplet or particulate flows. *AIChE J.* **25**, 843–855.

Jan, Y.-J. 1994 Computational studies of bubble dynamics. PhD Thesis, The University of Michigan.

Johnson, A. A. & Tezduyar, T. E. 1997 3D simulation of fluid-particle interactions with the number of particles reaching 100. *Comput. Methods Appl. Mech. Engng* **145**, 301–321.

Kim, I., Elghobashi, S. & Sirignano, W. A. 1993 Three-dimensional flow over two spheres placed side by side. *J. Fluid Mech.* **246**, 465–488.

Koch, D. L. 1993 Hydrodynamic diffusion in dilute sedimenting suspensions at moderate Reynolds numbers. *Phys. Fluids* A **5**, 1141–1155.

Koch, D. L. & Ladd, J. C. 1997 Moderate Reynolds number flows through periodic and random arrays of aligned cylinders. *J. Fluid Mech.* **349**, 31–66.

Ladd, A. J. C. 1993 Dynamical simulations of sedimenting spheres. *Phys. Fluids* A **5**, 299–310.

Ladd, A. J. C. 1997 Sedimentation of homogeneous suspensions of non-Brownian spheres. *Phys. Fluids* A **9**, 491–499.

Lafaurie, B., Nardone, C., Scardovelli, R., Zaleski, S. & Zanetti, G. 1994 Modeling merging and fragmentation in multiphase flows with SURFER. *J. Comput. Phys.* **113**, 134–147.

Lance, M. & Bataille, J. 1991 Turbulence in the liquid phase of a uniform bubbly air-water flow. *J. Fluid Mech.* **222**, 95–118.

Legendre D. & Magnaudet, J. 1998 Interaction between spherical bubbles rising side by side. *Third Intl Conf. on Multiphase flow, ICMF'98, Lyon, France, June 8–12.*

Loewenberg, M. & Hinch, E. J. 1996 Numerical simulation of a concentrated emulsion in shear flow. *J. Fluid Mech.* **321**, 395–419.

Magnaudet, J. M. 1997 The forces acting on bubbles and rigid particles. *ASME Fluids Engineering Division Summer Meeting, June 22–26.*

Manga, M. & Stone, H. A. 1993 Buoyancy-driven interactions between deformable drops at low Reynolds numbers. *J. Fluid Mech.* **256**, 647–683.

Maxey, M. R. & Patel, B. K. 1997 Forced-coupled simulations of particle suspensions at zero and finite Reynolds numbers. *ASME Fluids Engineering Division Summer Meeting, June 22–26.*

Mei, R. 1996 Velocity fidelity of flow tracer particles. *J. Fluid Mech.* **22**, 1–13.

Miyata, H. 1996 Time-marching cfd simulation for moving boundary problems. *21st Symp. on Naval Hydrodynamics, June 24–28, Trondheim, Norway*, pp. 1–21.

Pan, Y. & Banerjee, S. 1997 Numerical investigation of the effect of large particles on wall-turbulence. *Phys. Fluids* **9**, 3786–3807.

Qian, J., Tryggvason, G. & Law, C. K. 1997 An experimental and computational study of bouncing and deformation in droplet collision. *Phys. Fluids* (submitted).

Ryskin, G. & Leal, L. G. 1984 Numerical solution of free-boundary problems in fluid mechanics. Part 2. Buoyancy-driven motion of a gas bubble through a quiescent liquid. *J. Fluid Mech.* **148**, 19–35.

Saffman, P. G. 1973 On the settling speed of free and fixed suspensions. *Stud. Appl. Maths* **LII**, 115–127.

Sangani, A. S. & Didwania, A. K. 1993 Dynamic simulations of flows of bubbly liquids at large Reynolds numbers. *J. Fluid Mech.* **250**, 307–337.

Smereka, P. 1993 On the motion of bubbles in a periodic box. *J. Fluid Mech.* **254**, 79–112.

Squires, K. D. & Eaton J. K. 1990 Particle response and turbulence modification in isotropic turbulence. *Phys. Fluids* A **2**, 191–203.

Sussman, M., Smereka, P. & Osher, S. 1994 A level set approach for computing solutions to incompressible two-phase flows. *J. Comput. Phys.* **114**, 146–159.

Takagi, S. & Matsumoto, Y. 1994 Three-dimensional deformation of a rising bubble. *Proc. German-Japanese Symp. on Multiphase Flow* KfK 5389, p. 499.

Tomiyama, A., Sou, A., Žun, I. & Sakaguchi, T. 1994 Three-dimensional detailed numerical simulation of bubbly upflow in a vertical square duct. *Proc. German-Japanese Symp. on Multiphase Flow* KfK 5389, p. 487.

Truesdell, G. C. & Elghobashi. S. 1994 On the two-way interaction between homogeneous turbulence and dispersed solid particles. II: Particle dispersion *Phys. Fluids* A **6**, 1405–1411.

Unverdi, S. O. & Tryggvason, G. 1992*a* A front-tracking method for viscous, incompressible, multi-fluid flows. *J. Comput Phys.* **100**, 25–37.

Unverdi, S. O. & Tryggvason, G. 1992*b* Computations of multi-fluid flows. *Physica* D **60**, 70–83.

Wang, L. P. & Maxey, M. 1993 Settling velocity and concentration distribution of heavy particles in homogeneous isotropic turbulence. *J. Fluid Mech.* **256**, 27–68.

Yuan, H. & Prosperetti, A. 1994 On the in-line motion of two spherical bubbles in a viscous fluid. *J. Fluid Mech.* **278**, 325–349.

Zhang, D. Z. & Prosperetti, A. 1994 Averaged equations for inviscid disperse two-phase flow. *J. Fluid Mech.* **267**, 185–219.

Zhou, H. & Pozrikidis, C. 1993 The flow of ordered and random suspensions of two-dimensional drops in a channel. *J. Fluid Mech.* **255**, 103–127.

Zhou, H. & Pozrikidis, C. 1994 Pressure-driven flow of suspensions of liquid drops. *Phys. Fluids* A **6**, 80–94.

Zuber, N. 1964 On the dispersed two-phase flow in the laminar flow regime. *Chem. Engng Sci.* **19**, 897–917.